Chemical Research in Toxicology

Article

Cite This: Chem. Res. Toxicol. 2019, 32, 1599−1618

pubs.acs.org/crt

MoS_2-Modified Curcumin Nanostructures: The Novel Theranostic Hybrid Having Potent Antibacterial and Antibiofilm Activities against Multidrug-Resistant Hypervirulent *Klebsiella pneumoniae*

Ashish Kumar Singh,[†,‡,●] Himanshu Mishra,[§,●] Zeba Firdaus,[⊥,●] Shivangi Yadav,[†,●] Prerana Aditi,[⊥] Nabarun Nandy,[¶] Kavyanjali Sharma,[#] Priyanka Bose,[‖] Akhilesh Kumar Pandey,[‡] Brijesh Singh Chauhan,[‡] Kaushik Neogi,[□] Kunwar Vikram,[○,△] Anchal Srivastava,[§] Amrita Ghosh Kar,[#] and Pradyot Prakash*[,†]

[†]Bacterial Biofilm and Drug Resistance Research Laboratory, Department of Microbiology, Institute of Medical Sciences, [‡]Department of Biochemistry, Institute of Science, [§]Nano Research Laboratory, Department of Physics, Institute of Science, [⊥]Department of Medicinal Chemistry, Institute of Medical Science, [¶]Cytogenetics Laboratory, Department of Zoology, Institute of Science, [#]Department of Pathology, Institute of Medical Sciences, [‖]Department of Chemistry, Institute of Science, and [□]Department of Pharmaceutical Engineering and Technology, Indian Institute of Technology, Banaras Hindu University, Varanasi 221005, India

[○]Department of Physics, Indian Institutes of Sciences, Bangalore 560012, India

[△]Graphic Era University, Dehradun 248002, India

Supporting Information

ABSTRACT: The recent emergence of hypervirulent clinical variants of *Klebsiella pneumoniae* (hvKP) causing community-acquired, invasive, metastatic, life-threatening infections of lungs, pleura, prostate, bones, joints, kidneys, spleen, muscles, soft-tissues, skin, eyes, central nervous system (CNS) including extrahepatic abscesses, and primary bacteremia even in healthy individuals has posed stern challenges before the existing treatment modalities. There is therefore an urgent need to look for specific and effective therapeutic alternatives against the said bacterial infection or recurrence. A new type of MoS_2-modified curcumin nanostructure has been developed and evaluated as a potential alternative for the treatment of multidrug-resistant isolates. The curcumin quantum particles have been fabricated with MoS_2 via a seed-mediated hydrothermal method, and the resulting MoS_2-modified curcumin nanostructures (MQCs) have been subsequently tested for their antibacterial and antibiofilm properties against hypervirulent multidrug-resistant *Klebsiella pneumoniae* isolates. In the present study, we found MQCs inhibiting the bacterial growth at a minimal concentration of 0.0156 μg/mL, while complete inhibition of bacterial growth was evinced at concentration 0.125 μg/mL. Besides, we also investigated their biocompatibility both *in vitro* and *in vivo*. MQCs were found to be nontoxic to the SiHa cells at a dose as high as 1024 μg/mL on the basis of the tested adhesion, spreading of the cells, and also on the various serological, biochemical, and histological investigations of the vital organs and blood of the Charles Foster Rat. These results suggest that MQCs have potent antimicrobial activities against hvKP and other drug resistant isolates and therefore may be used as broad spectrum antibacterial and antibiofilm agents.

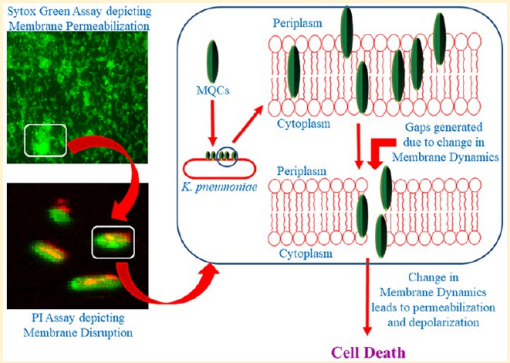

1. INTRODUCTION

The last two decades have witnessed the emergence of hypervirulent *Klebsiella pneumoniae* (hvKP), a new clinical variant.[1] Unlike the "classical" *K. pneumoniae* (cKP), it causes community-acquired pyogenic liver abscess (CAPLA) and intriguingly causes septic metastatic spread to distant sites in the majority of cases (as high as 80% of cases). Although hvKP infect(s) all races, the majority of cases have been reported among Asians exhibiting a very high mortality ranging from 3−42%.[2] The situation becomes more intricate with survivors of metastatic spread leading to the manifestation of ruinous morbidities such as loss of vision and neurologic sequelae. Metastatic spread is a common feature among Gram-positive pathogens such as *Staphylococci* and *Streptococci* but is uncommon among enteric Gram-negative pathogens.[3] From a clinical perspective, hvKP management becomes more important due to its associated high morbidity and mortality among healthy individuals. The detection of hvKP is somewhat

Received: March 29, 2019
Published: July 18, 2019

DOI: 10.1021/acs.chemrestox.9b00135
Chem. Res. Toxicol. 2019, 32, 1599−1618

empirical, identified by a positive "string test." Increased capsule production is one of the hallmarks of hvKP.[4]

Curcumin is one of most studied polyphenols, which has found its applications in almost all realms of therapeutics. A plethora of studies on the assessment of its biological role have been conducted, of which its antibacterial and antibiofilm properties are of significant medical implications especially in the current scenario of scarce therapeutic alternatives.[5] Recently, our group has documented almost 90-times improved efficacy of quantum curcumin as an antibacterial and antibiofilm agent against *S. aureus*, *S. epidermidis*, *E. coli*, and *K. pneumoniae* compared to its native form.[6] Besides, another recent report documents its high efficacy of inhibition in quantum form against the major virulence factor of *P. gingivalis*: gingipains R and K.[7] The application of quantum dot (QDs)-based chemotherapy is based on the concept that hypervirulent biofilm indwellers tend to develop hyper-viscous microenvironments and, thus, provide selective access for quantum particles.[1] The advantage with QDs due to their enhanced permeability and retention (EPR) effect has become the governing principle of our current work. However, the utility of quantum dots as medicine has recently been challenged due to their low distribution across the biofilms and the lack of evidence supporting the biocompatibility of QDs.[8] Biofilm heterogeneity (compositional differences due to inter and intrasubject differences) possibly poses potential limitations to the distribution of QDs.

Molybdenum disulfide, a member of transition metal dichalcogenides (TMDs) family, has been explored much as an alternative of graphene in its 2D as well as 0D (QDs) forms.[9] Interestingly, molybdenum disulfide quantum dots (MoS_2-QDs) exhibit intense fluorescence, high photostability, size tunability, lesser toxicity, and hence better biocompatibility.[10] Several reports document its use as bioimaging probe both *in vivo* and *in vitro*. A recent report from Mishra et al. also proves its utility as a bioimaging material in the dose as high as 80 μL/mL in Drosophila.[11] Because of its high water dispersibility and stability, it has found another application as MoS_2 nanoflower and polyethylene glycol based system, to show the enhanced antibacterial activity.[12] Hydrothermally synthesized ZnO-MoS_2 nanosheets structures have shown better antibacterial activity than the ZnO and MoS_2 nanosheets alone.[13] Curcumin does not enter the bacterial cells directly, which increases its MIC indices against the otherwise sensitive strains as well. However, there are reports for MoS_2 QDs related to their abilities to enter the cells and hence utilization for bioimaging. Therefore, both curcumin and MoS_2 were hybridized as MoS_2-modified curcumin nanostructures (MQCs) to make them enter the cell so that it could penetrate across the width of cell membrane without completely entering the cell for its therapeutic exploitations. In view of these promising merits of MoS_2 and the curcumin, we perceived prudence of using MoS_2 and curcumin together for specific applications when the antibacterial and antibiofilm properties against the said pathogen are simultaneously required.

Reports suggest that the composition, structure, and shape of the nanomaterials can be tuned as per need to augment their therapeutic competence.[9] Cells have different capabilities of sensing different nanostructures, which may elicit altogether different cellular responses.[14−16] Therefore, the utilization of nanostructures as a newer therapeutic modality is in vogue. Realization of the various merits and scarce therapeutic options against multidrug-resistant hypervirulent *Klebsiella* isolates necessitated the attempt to combine MoS_2 with the curcumin for its potential applications to curb the menace orchestrated by the said pathogen.

In the present study, we, for the first time, designed and synthesized MoS_2-modified curcumin nanostructures (MQCs) and evaluated for its antibacterial and antibiofilm properties. To achieve this goal, MQCs were fabricated via a facile ecofriendly seed-mediated hydrothermal synthesis method. The composition and structures of these MQCs were characterized, and the therapeutic effects were evaluated against drug-resistant isolates. Subsequently, we investigated the mode of action of MQCs against the MDR isolates of hvKP *Klebsiella pneumoniae*. Besides, a detailed biocompatibility profile was investigated both *in vitro* and *in vivo*. For *in vitro* analysis, we mainly utilized sulforhodamine B assay for cell proliferation, and hemocompatibility assay and lactate dehydrogenase assay for membrane integrity analysis, while *in vivo* biocompatibility was tested utilizing Charles Foster Rats investigated for its hematological/serological profiling, lipid peroxidation, superoxide dismutase activity, and catalase activity with subsequent validation by histopathological screenings.

2. MATERIALS AND METHODS

2.1. Chemicals and Materials. Curcumin (>95% pure) was procured from TCI chemicals, Japan. Sodium molybdate dihydrate ($Na_2MoO_4{\cdot}2H_2O$) and L-cysteine ($C_3H_7NO_2S$) were purchased from HiMedia laboratories, India. Hydrochloric acid (HCl) and ethanol (C_2H_5OH) were purchased from Molychem, India. All the purchased chemicals were of analytical grade and were used without any further purification. For solution preparation during the entire study, deionized (DI) water (MiliQ, Millipore) was used. Phosphate buffered saline (PBS, pH 7.2) and Tris-HCl buffer (pH 7.6) were prepared in-house, while Dulbecco's modified Eagle's medium, DABCO, and propidium iodide from Life technologies, Invitrogen were used. Flat-bottom polystyrene 96-well tissue culture plates and eight-well chambered slides were procured from SPL biosciences, Korea. Penicillin, streptomycin, and gentamycin were from SRL laboratories, India, while Hanks balanced salt solution (HBSS), heparin, sodium bicarbonate, dimethyl sulfoxide (DMSO), 3,3′-dipropylthiadicarbocyanine iodide ($DiSC_3$-5) and 1,6-diphenyl-1,3,5-hexatriene (DPH) were from Sigma-Aldrich, USA. Trisodium citrate, calcium chloride ($CaCl_2$), crystal violet (CV), hydrogen peroxide (H_2O_2), butylated hydroxyl toluene (BHT), sodium dodecyl sulfate (SDS), thiobarbituric acid (TBA), butanol, pyridine, L-methionine, hydroxylamine hydrochloride, ethylene diamine tetraacetate (EDTA), riboflavin, sodium azide, NADPH, 85% phosphoric acid, and acetone were procured from Merck, USA, while paraformaldehyde and brain heart infusion (BHI) broth were procured from HiMedia laboratories, India. Bradford reagent supplied by Bio-Rad, USA was used for all protein estimations.

2.2. Synthesis and Fabrication of MoS_2 Modified Curcumin Quantum Dots. MoS_2−curcumin (MQC) nanostructures have been synthesized using a seed-mediated facile and eco-friendly hydrothermal method described earlier with modifications.[9,11] In a typical synthesis method, 0.25 g of sodium molybdate dihydrate and 0.50 g of L-cysteine were taken in 25 and 50 mL of DI water, respectively, in two separate beakers and stirred for 10 min at 40 °C to dissolve with subsequent mixing of either solution in another beaker at pH ≈ 5. This was followed by the addition of 10% ethanol such that the cumulative volume of the solution remained 90 mL. Curcumin (2:1 wt % ratio) was subsequently added to the solution with stirring for 10 min at 40 °C. The final solution was then transferred to stainless steel lined Teflon autoclave of capacity 100 mL and was put into an oven maintained at 220 °C for hydrothermal reaction for the next 36 h. After the completion of the reaction, a light yellowish colloidal solution containing MQCs was eluted. The obtained colloidal solution was then spun at 10 000 rpm for 60 min, and the obtained supernatant was subsequently used for further studies.

DOI: 10.1021/acs.chemrestox.9b00135
Chem. Res. Toxicol. 2019, 32, 1599−1618

2.3. Structural Characterizations. The structural properties of the sample were investigated using high-resolution transmission electron microscopy (HRTEM, FEI-Technai G^2 F20) operated at an accelerated voltage 200 kV. The thickness and size of the sample have been tested using atomic force microscopy (Bruker Veeco Innova, USA) in noncontact/tapping mode. For atomic force microscopic characterization, the sample was deposited on SiO_2/Si substrate using spin coating method at 8000 rpm and dried in the open air at 50 °C. Further, the sample was characterized spectroscopically using Raman spectrometer (Renishaw in-Via spectrometer, UK) and FTIR-ATR spectra acquisition. The FTIR-ATR spectrum was generated in mid-IR mode, equipped with a Universal ATR (attenuated total reflectance) sampling device containing diamond/ZnSe crystal. The spectra were scanned at room temperature in transmission mode over the wavenumber range of 4000 to 650 cm^{-1}, with a scan speed of 0.20 cm/s, and 30 accumulations at a resolution of 4 cm^{-1}. Photophysical characterizations were performed using UV−vis absorption spectrometer (PerkinElmer, USA) with 10 mm optical path length, photoluminescence spectrometer (PerkinElmer, USA), time-resolved photoluminescence spectrometer (FLS920, Edinburgh, UK). For structural composition and surface chemical states, the sample has been characterized using X-ray photoelectron spectroscopy (XPS) on an ESCA Lab 250Xi (Thermo Scientific, USA) with 200 W monochromatic Al K_α radiation.

2.4. Antibacterial Investigations. *2.4.1. Bacterial Strains and Culture Conditions.* The multidrug resistant hypervirulent (hv MDR) clinical isolate of *Klebsiella pneumoniae* [Lab code: 2886/2018 (from blood), 10825/2018 (from urine), 197/2018 (from stool), 1739/2018 (from pus)], Methicillin-sensitive *Staphylococcus aureus* (Lab code: 1632/2018, MSSA), Methicillin-resistant *Staphylococcus aureus* (MRSA, lab code: 699/2018), and *Pseudomonas aeruginosa* (Lab code: 2564/2018) were investigated in this study. Besides, investigations against select control bacterial strains namely *Staphylococcus aureus* (ATCC 29213), *Klebsiella pneumoniae* (ATCC 700603), and *Pseudomonas aeruginosa* (ATCC 25619) were done.

However, the study was focused primarily on hv MDR *Klebsiella* isolates having heterogeneous biofilm matrix compositions with regard to the proportion of sugars and proteins. The bacterial identification was performed using conventional bacteriological techniques such as colony morphology, gram-staining, and different biochemical tests described elsewhere.[6] We defined multidrug resistance in the present study as absolute resistance against at least five different classes of drugs. Antibiotic susceptibility testing of the isolates was performed by modified Kirby−Bauer method in accordance with the Clinical and Laboratory Standards Institute guidelines 2018. We used 14 antibiotic discs, namely Ampicillin (10 μg), Amikacin (30 μg), Amoxicillin/clavulanate (20/10 μg), Levofloxacin (5 μg), Cephalexin (30 μg), Cefuroxime (30 μg), Gentamicin (120 μg), Ciprofloxacin (5 μg), Cefepime (30 μg), Co-trimoxazole (23.75/1.25 μg), Piperacillin and tazobactam (100/10 μg), Ertapenem (10 μg), Meropenem (10 μg), and Imipenem (10 μg).

2.4.2. Minimum Inhibitory Concentration (MIC) Determination. The minimum inhibitory concentration of MQC was determined against the aforementioned isolates by the broth microdilution method as described earlier with minor modifications.[6]

Briefly, the above-mentioned bacteria were grown in 10 mL of BHI broth aerobically for 18 h. Bacterial culture (500 μL) was then diluted to 1.5 mL of fresh BHI broth. The freshly prepared MQC stock solution (50 μg/mL) was used for the study. The stock was diluted in a series of two-fold dilutions ranging from 0.098 to 25 μg/mL in sterile BHI broth in microtiter wells. Each well of the 96-well microtiter plate was then inoculated with 190 μL of standardized cell suspension (10^5 CFU/mL) and incubated at 37 °C for next 18 h along with the 20 μL drug suspension. The MIC was defined as the lowest concentration of MQC at which no perceivable growth was observed. Positive controls were devoid of any drug moiety, while the sterile broth was used as negative control, and all the experiments were performed in triplicate. Besides, we verified the results by investigating the reduction in colony forming units utilizing Gompertz analysis as described elsewhere.[17,18]

2.4.3. Bacterial Growth Curve Analysis. The effect of MQCs on growth rates of the respective bacterial isolates was analyzed spectrophotometrically employing Synergy H1 Hybrid Multi-Mode Reader in both the presence and absence of the drug as described previously.[7] Briefly, the bacterial cells at early exponential phase were inoculated into TCP such that its OD at λ_{max} 600 nm was approximately 0.01. The optical density of each well was then monitored at this wavelength by periodic measurements after every 15 min for 4.5 h in either of the situations. The growth rate was determined by the slope of the linear part of the growth curve (R^2, ≥0.98), determined for at least five data points of the semilogarithmic plot of absorbance (ln [OD600]) versus incubation time (in hours).

2.4.4. Antibiofilm Activity Determination. 2.4.4.1. Tissue Culture Plate Assay (TCP). The antibiofilm assay was performed in 96-well tissue culture plate as described previously with minor modifications.[19] Briefly, an overnight culture of *Klebsiella pneumoniae* (Lab code: 10825/2017) was grown in Luria−Bertani broth. A volume of 180 μL of each diluted bacterial suspension (0.5 McFarland's) was dispensed into flat-bottom polystyrene 96-well tissue culture plate and 20 μL of MQC solution (50 μg/mL) was added to each well. Wells without MQCs were set up as controls. Plates were incubated at 37 °C without shaking for 18 h in one case where its biofilm inhibitory actions were investigated, whereas degradation effects of the hybrid quantum dot investigated over 72 h old antecedently formed biofilm by incubating for 180 min. After respective incubations, biofilm was quantitated by crystal violet (CV) assay as described earlier. The assays were performed in triplicate, and the results were expressed as mean OD_{570} ± the standard deviation of the mean (SD): % Reduction = (Mean Absorbance of Control − Mean Absorbance of Test Sample)/(Mean Absorbance of Control) × 100.

2.4.4.2. Confocal Laser Scanning Microscopy for Determination of Antibiofilm Properties. For confocal analysis of the effects of MQCs, we grew *K. pneumoniae* biofilm in chambered slides as described previously.[7,20] Briefly, *K. pneumoniae* (lab no.10825/2018) was grown in BHI broth overnight and was then diluted 1:100 in fresh BHI broth such that absorbance was adjusted to 0.2 at λ_{max} 600 nm. Twenty microliters of its diluted suspension was then dispensed into an eight-well flat-bottom chambered slide containing 480 μL of BHI broth. The biofilm was statically grown for 72 h. This was followed by time-dependent treatment with 0.05 μg/mL MQCs. Prior to staining, the residual broth was removed by gentle tapping and washed thrice by phosphate buffer (pH 7.5). Biofilm was fixed using 4% (v/v) paraformaldehyde for 30 min. The PI was reconstituted with DMSO, and the stock solution of 1 mg/mL was prepared and stored frozen in aliquots of 100 μL. For use, stock solutions were diluted with phosphate buffer to the concentration of 10 μg/mL. Ten-microliter samples of these staining solutions were applied directly to the top of the biofilms.

The Zeiss LSM 510 inverted confocal laser-scanning microscope (Carl Zeiss, Jena, Germany) was used to detect the green and red fluorescence from the dyes. Propidium iodide was excited with the HeNe2 530 nm laser, and emission fluorescence was collected with the 620 nm filter. Images were obtained via a Plan-Neofluar 40×/1.3 oil objective with a z-step of 2.0 μm or 20× objective with a z-step of 5.0 μm.

2.5. Mechanistic Insights to Antimicrobial Activities. *2.5.1. Study of Changes in Membrane Dynamics.* Multidrug-resistant hv *K. pneumoniae* isolate (lab no. 10825/2018) was treated with MIC concentration of MQCs. The treated cells were incubated for 2 h with shaking (100 rpm) at 37 °C, harvested, resuspended, pelleted, and fixed with 0.4% paraformaldehyde. Subsequently, the final cell pellets were resuspended in PBS. To evaluate the change in membrane dynamics, we targeted the lipid acyl groups as described earlier.[21] The resuspended cells were incubated with 0.5 mM 1, 6-diphenyl-1,3,5-hexatriene (DPH) at 37 °C for 60 min, pelleted, and washed thrice with PBS. The fluorescence intensity was monitored spectrophotometrically by employing Synergy H1 Hybrid Multi-Mode Reader at 350 nm (excitation) and 425 nm (emission).

2.5.2. Membrane Permeabilization Assay. We hypothesized the membrane permeabilization to be the mode of action of MQCs. We measured it by conducting the Sytox Green uptake assay.[22] Briefly,

DOI: 10.1021/acs.chemrestox.9b00135
Chem. Res. Toxicol. 2019, 32, 1599−1618

MDR hv *Klebsiella* isolate was cultured overnight in Muller Hinton Broth and then diluted in 5 mM HEPES buffer such that OD was adjusted to 0.2 at λ_{max} 600 nm. A total of 50 μL of MIC concentration MQCs was added to the bacterial suspension in a 96-well plate. Subsequently, this suspension was mixed with 50 μL of Sytox Green (5 μM, 1:1). We utilized fluorescent microscopy for observing the direct uptake of Sytox Green as the method described earlier for confocal microscopy.

2.5.3. Membrane Depolarization Assay. The membrane potential-sensitive dye $DiSC_3$-5 was used to measure plasma membrane depolarization/electrical potential disturbance in bacterial membranes as described previously.[23] *K. pneumoniae* isolate was cultured in BHI broth overnight. The bacterial culture was then diluted such that OD was adjusted to 0.05 at λ_{max} 600. This was followed by the addition of 50 μL of MIC concentration MQCs for 2 h at 37 °C. The test sample and the controls (negative control was without any drug, while positive control was treated with CCCP) were subsequently incubated for 20 min with 1 μM $DiSC_3$-5. The fluorescence was measured employing Synergy H1 Hybrid Multi-Mode Reader with excitation at 622 nm and emission at 670 nm. Besides, the intensity and the percentages of bacterial cells showing fluorescence were measured using the flow cytometry (Becton−Dickinson, San Jose, CA, USA).

2.5.4. 2′,7′-Dichlorfluorescein-diacetate (DCFH-DA) Analysis for ROS Production in Bacteria Using Flow Cytometry. Endogenous reactive oxygen species (ROS) production in bacteria after the exposure of MQCs for 48 h was monitored by flow cytometry using 2′,7′-dichlorofluorescein-diacetate (DCFH-DA) as ROS marker described earlier.[7] Post exposure for 48 h, the bacterial cells were harvested upon centrifugation at 3000*g* for 30 min. The bacterial pellet was washed thrice with phosphate-buffered saline (PBS, pH ≈ 7.2), and then cell density was adjusted to 10^6/mL by suspending the cells in PBS. The resuspended cells were then incubated for 30 min with 5 μM DCFH-DA followed by analysis of ROS production on a BD Accuri C6 Flow cytometer. The data acquisition was performed with BD Accuri C6 software based on light-scatter and fluorescence signals resulting from 20 mW laser illumination at 488 nm. All the measurements were performed logarithmically. The assay was performed at a low sample rate (14 μL min^{-1}). A total of 10 000 000 events were taken into account for each sample.

2.5.5. In Silico Docking Study. Docking was performed using combined energy evaluation through precalculated grids of affinity potential employing various search algorithms to find the suitable binding position for a ligand on a given protein (LOX) for both AutoDock and Vina docking software. All rotatable bonds in the ligands were kept free to allow flexible docking. Grid size was set to 60× 60 × 60 grid points (x, y, and z), with spacing between grid points kept at 0.375 Å. The grid box was generated using the axis details from ligand explorer for specification and precision controlling center grid box.[24] The Lamarckian genetic algorithm was chosen to search for the best conformers.[25]

For AutoDock, a set of 250 independent docking runs were generated using genetic algorithm search. AutoDock analyzer analyzed the outcomes of results; the complex .pdb file was investigated in the discovery studio visualizer 2017 for better interpretation. The best interacting conformer with least binding energy is reported as the final result. However, for Vina, a set of 10 independent docking runs for 20 times and a set of conformers was generated to produce a population of 150 using genetic algorithm search. AutoDock analyzer using the pdbqt files analyzed the outcomes of results, the result complex .pdb file regarding the classical hydrophobic interaction between the macromolecule, and the ligand moiety was investigated in the discovery studio visualizer 2017. Docking method used is the standard method reported, and the best interacting conformer with least binding energy was concluded as the result.

2.6. *In Vitro* Evaluation of Cytotoxicity. The freshly prepared MQCs and MoS_2 QDs were further utilized for comparative evaluation of their toxicity profiles. Prior to the experiment, all the QDs were dispersed by ultrasonication for about 15 min with a power input of 750 W, frequency 10 kHz, and intensity 30 W/cm^2 in pulse ratio on/off 50:10 (s/s).

2.6.1. Cell Culture. SiHa cells were cultured in Dulbecco's modified Eagle's medium supplemented with 10% fetal bovine serum along with 100 U/mL penicillin and 100 mg/mL streptomycin in a 5% CO_2 humidified atmosphere at 37 °C in a CO_2 incubator. The cells were exposed to both quantum dots for 24 h. A 2 mg/mL stock solution of MoS_2 and MQCs quantum dots were prepared and were stored as small aliquots at 4 °C and diluted two-fold in a different dose ranging from 2 to 1024 μg/mL in Dulbecco's modified Eagle's medium.

2.6.2. Cell Proliferation Assay. Cell proliferation was determined using the sulforhodamine B (SRB) assay as described previously.[26] The proliferating SiHa cells were seeded into 96-well plates at a density of 5 × 10^3 cells per well and allowed to adhere overnight. Twenty-four hours later, cells were incubated for 48 h with a range of concentrations of MQCs and MoS_2 quantum dots (2−1024 μg/mL). Cells were fixed with 50% (w/v) TCA and stained with 0.4% (w/v) sulforhodamine B (SRB) for 30 min before washing with 1% (v/v) acetic acid. SRB was solubilized with 10 mM Tris pH ≈ 10.5, the absorbance read at 510 nm, and cell growth expressed as the percentage (%) of the growth of untreated cells. The concentration of QDs that resulted in 50% growth inhibition (GI50) was calculated by interpolation from the growth inhibition versus concentration curves using GraphPad Prism version 5.01 for Windows (GraphPad Software Inc., USA).

2.6.3. Lactate Dehydrogenase Assay. The comparative cytotoxicities of MoS_2 and MQCs quantum dots were evaluated using SiHa cells by measuring lactate dehydrogenase (LDH) activity as described earlier.[7,27] The two discrete classes of QDs were evaluated in concentration range of 2, 4, 8, 16, 32, 64, 128, 256, and 512 to1024 μg/mL. Briefly, the 12 h treated cells were spun at 400*g* for 5 min, and the growth medium was collected. The broth and the LDH reagent were incubated in the ratio of 2:1 for 30 min followed by the absorbance reading at 500 nm. For control, we used 2% Triton X treated cells. The extent of percentage (%) cytotoxicity was calculated as follows: % Cytotoxicity = (Mean Absorbance of Treated Cells − Absorbance of Medium − Absorbance of Cell and Medium)/(Absorbance of Triton X Treated Cell − Absorbance of Cell and Medium × 100.

2.7. *In Vivo* Evaluation of Cytotoxicity. *2.7.1. Animal.* We procured total thirty-six Charles Foster strain rats (male, 100−120 g) from central animal house, Banaras Hindu University and maintained them at 25 °C under a standard regimen of 12 h:12-h light−dark cycle. We chose male rats to avoid any metabolic variation(s) due to gender such as sex hormone, lactation, and pregnancy. Rats were kept separately in propylene cage and fed standard pellet diet under hygienic conditions. Prior to the start of the experiment, the animals were acclimatized to the experimental environment for 1 week. Ethical guidelines were strictly followed for care and use of rats, which were approved by the Institutional Animal Ethics Committee (IAEC), Banaras Hindu University, India (Ethical committee letter No. 2017/CEC/720).

Post acclimatization, rats were randomly divided into six groups such that each group contains six rats. One of the groups (Group I) was selected as the negative control (MiliQ water), while another constituted the positive control (1024 μg/mL MoS_2 QDs, Group II), and the remaining four groups (Group III−VII) were set as the experimental groups.

After the first dose, we made general observations like changes in body weight, activity, and physical appearance for the first 24 h, with keen observation in the first 4 h, and then for 14 days. On the 15th day, all rats were euthanized to collect the whole blood for hematological and serum biochemical assays. Liver, kidney, and spleen were excised aseptically and weighed. Half part of the organs was stored in 10% formalin for histological studies and remaining half was stored at −80 °C for biochemical study. At the time of the experiment, 10% tissue homogenate (w/v) was prepared in 1 M phosphate buffer (pH 7.4) containing 0.1 mM EDTA using a motor-driven Teflon-pestle homogenizer (Fischer-Scientific). Homogenate was centrifuged at 3000*g* for 15 min at 4 °C. Pellet was discarded, and the supernatant was recentrifuged at 7500*g* for 20 min at 4 °C. The supernatant was collected and used for biochemical estimations of alanine aminotransferase (ALT), aspartate aminotransferase (AST), glucose, alanine aminotransferase, aspartate aminotransferase, creatinine, and urea.

DOI: 10.1021/acs.chemrestox.9b00135
Chem. Res. Toxicol. 2019, 32, 1599−1618

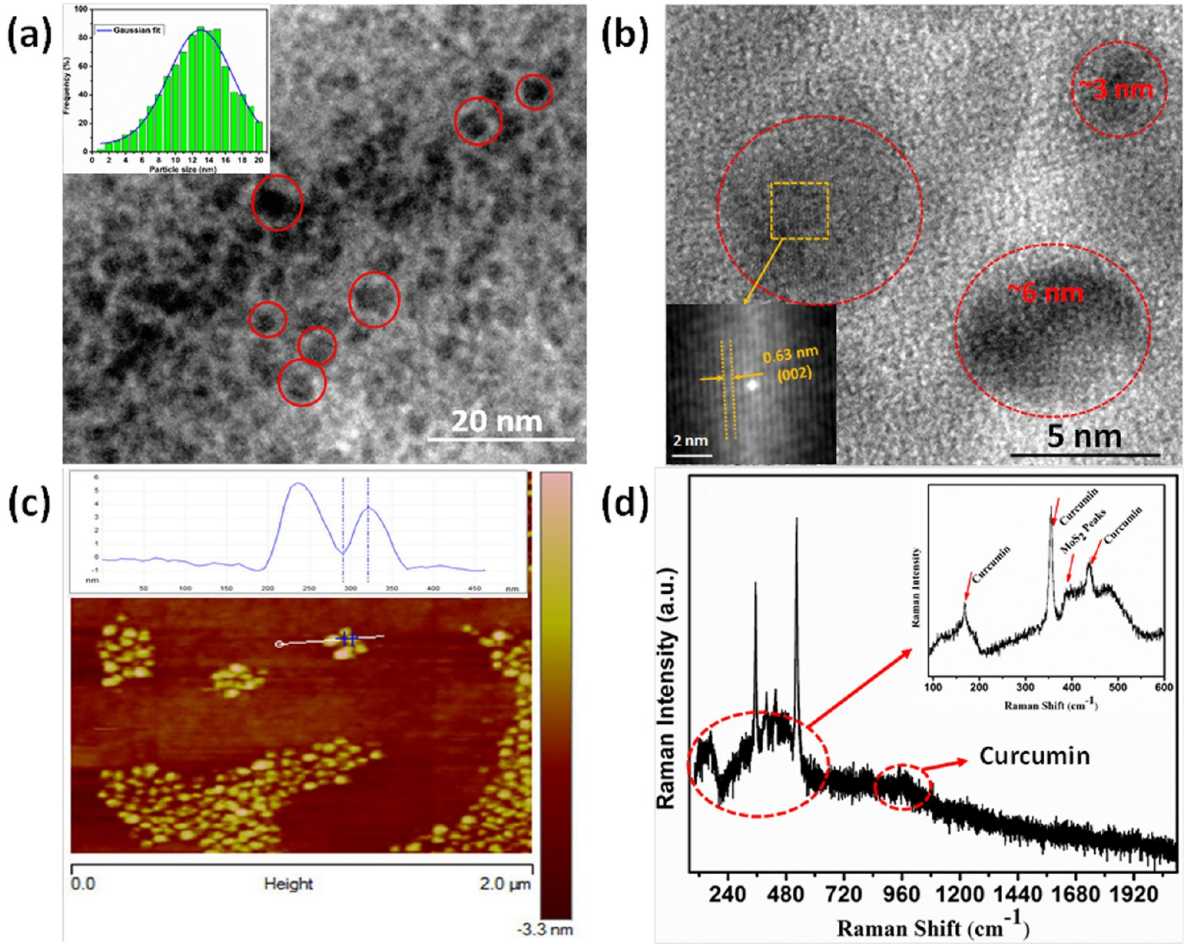

Figure 1. (a) TEM image of MQC, inset shows the particle distribution bar diagram fitted for a Gaussian function, (b) HRTEM image of MQC, inset showing an interlayer spacing of ~0.63 nm corresponding to the (002) plane of MoS_2, (c) AFM image of MQC, and (d) Raman spectrum of MQC, inset shows the enlarged view of Raman peaks appearing lower wavenumber side (<500 cm^{-1}).

Total hemoglobin was also estimated using Hemocor D kit. SOD and catalase assays were performed manually for serum. Analyses of blood parameters were also done. From tissues, we also estimated lipid peroxidation, SOD, and catalase (for detailed method, refer to Supporting Information 3).

2.7.2. Histopathological Investigation. The excised portion of the tissues was washed with ice-cold normal saline (0.9% NaCl) and 20 mM EDTA to remove blood traces and then immediately fixed in 10% formalin for 72 h. The tissues were then transferred and stored in 70% ethanol. The tissue specimens (liver, kidney, spleen) were then embedded in paraffin and diced into 0.5 μm thicknesses blocks followed by mounting and staining with hematoxylin and eosin (HE) for histopathological examination under an optical microscope. At least 10 slides per sample were prepared and subjected to histopathological evaluations.

2.8. Statistical Analysis. All the experiments were performed in triplicate, and the data were based on an average of the three different experiments. The data were expressed as mean values with the corresponding standard deviations (SD). Statistical significance was analyzed by one-way analysis of variance (ANOVA) applying Dunnett's post hoc test. Besides, Mann–Whitney U test and Student's *t* test (two-tailed, unequal variance) were also done. The data obtained from animal studies were analyzed by using ANOVA for multiple comparisons followed by Newman- keul post hoc analysis. All the statistical calculations were done using GraphPad Prism version 5.1 (GraphPad Software, Inc., La Jolla, CA, USA). We considered *P*-value of <0.05 as statistically significant.

3. RESULTS AND DISCUSSION

3.1. Structural Characterizations. Figure 1a shows the TEM image of MQCs. MQCs are encircled with red color. The inset of Figure 1a shows the particle distribution histogram estimated over ~200 particles. The particle distribution histogram has been fitted for Gaussian function, and the average particle size is found to be ~13 nm. MQCs are larger than the hydrothermally synthesized MoS_2-QDs may be due to the wrapping of MoS_2 over curcumin. HRTEM of nanostructures has been shown in Figure 1b. The inset shows an interlayer spacing of ~0.63 nm corresponding to the (002) plane of MoS_2. MQCs were spin coated over SiO_2/Si substrate and dried in the open air at 50 °C before performance of AFM characterizations in noncontact/tapping mode (Figure 1c). AFM measurement suggests a lateral size of ~24 nm and thickness of ~4 nm. Raman spectra of MQC recorded for an excitation wavelength ~663 (= 1.87 eV) nm are shown in Figure 1d. The inset shows the Raman spectrum within wavenumber range 100 cm^{-1} to 600 cm^{-1}, which shows several Raman peaks corresponding to MoS_2 and curcumin. A small Raman signal is obtained at ~963 cm^{-1} corresponding to curcumin. There is no Raman signal in the high wavenumber range (≥1000 cm^{-1}) corresponding to curcumin, which may be due to the fluorescence of MoS_2-QDs. The whole mechanism behind this and PL spectra of MoS_2-QDs at excitation wavelength ~663 nm has been

DOI: 10.1021/acs.chemrestox.9b00135
Chem. Res. Toxicol. 2019, 32, 1599–1618

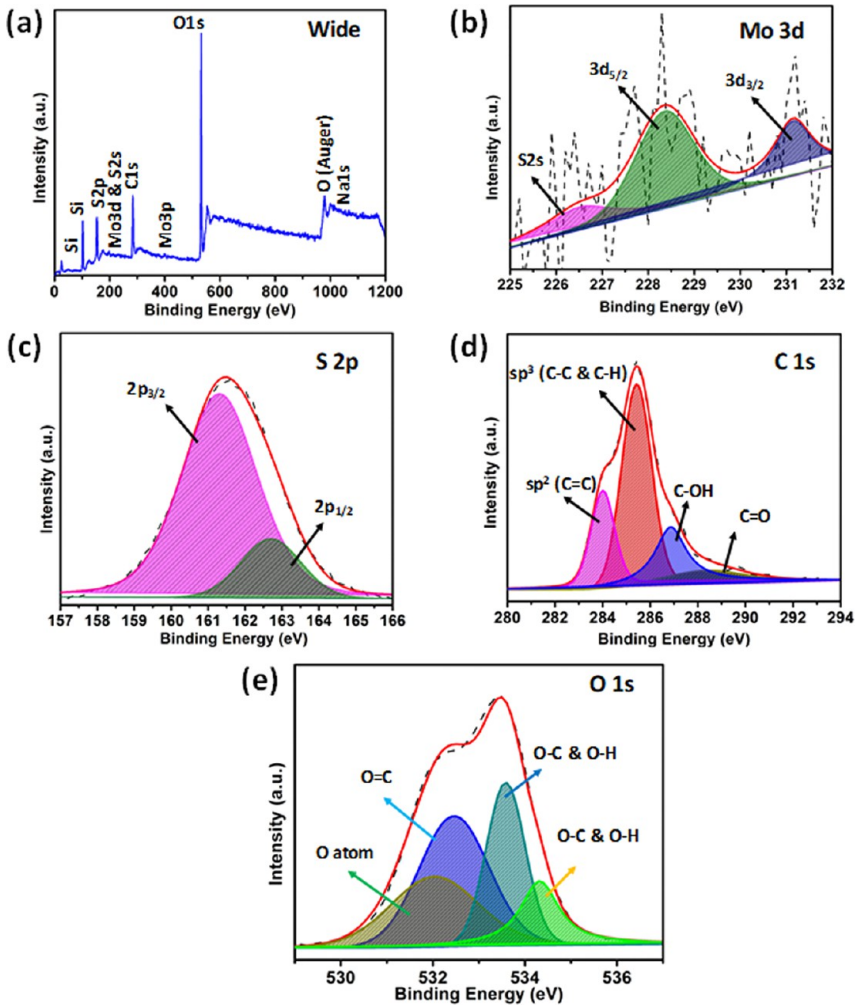

Figure 2. (a) Wide scan and high resolution (b) Mo 3d, (c) S 2p, (d) C 1s, and (e) O 1s XPS survey of MQC.

explained in the Supporting Information (Supporting Information 1, Figure S2).

3.1.1. X-ray Photoelectron Spectroscopy (XPS) Characterization. To investigate the surface composition, XPS characterization was performed (Figure 2). Figure 2a shows the wide range XPS survey, which consists of Mo and S along with C, O, Na, etc. High-resolution XPS (HRXPS) spectra are shown in Figure 2b–e. HRXPS spectrum for Mo 3d can be deconvoluted into three different peaks at positions ∼226.5, 228.4, and 231.2 eV corresponding to S 2s, $3d_{5/2}$, and $3d_{3/2}$ orbital binding energy, respectively (Figure 2b). Figure 2c shows the HRXPS of S 2p orbitals, which can be deconvoluted into two peaks at positions ∼161.3 and 162.7 eV, respectively. These two deconvoluted peaks correspond to $2P_{3/2}$ and $2P_{1/2}$ orbitals binding energy, respectively. HRXPS of C 1s is deconvoluted into four peaks of binding energies ∼284.0, 285.5, 286.8, and 288.8 eV, respectively. These four deconvoluted XPS peaks correspond to sp^2 (C═C), sp^3 (C−C and C−H), C−OH, and C═O binding energies. The presence of C−OH and C═O at binding energies ∼286.6 and 288.8 eV confirms the presence of −OH and −COOH functional groups over the surface of the MQC. HRXPS of O 1s is shown in Figure 2e where four peaks appear at positions ∼532, 532.4, 533.6, and 534.3 eV, respectively. These peaks correspond to surface adsorbed oxygen atoms, O═C and O−C, and O−H, respectively. The presence of O−H and O−H peaks again confirmed the functionalization of MQC.

3.2. Photophysical Characterizations of MQC. UV−vis absorption spectra of the MoS_2 and MQCs are depicted in Figure 3a. For curcumin, absorption bands appeared at ∼427 and 277 nm, respectively, while for MoS_2, it appeared at ∼388 nm. The absorption spectrum of MQC displayed absorption band at ∼392 and 319 nm along with a hump at ∼452 nm. For MQCs, the strong absorption maximum was found at around 452 nm with an absorption onset at 370 nm confirming the presence of curcumin. As compared to native curcumin, the position of the curcumin peak in MQCs exhibited bathochromic shift. The curcumin showed a main absorption band of $\pi-\pi^*$ transition at 415−430 nm and compared to native curcumin, the MQCs showed maximum absorption shifted by (∼25 nm), which indicated the involvement of the carbonyl group of curcumin in metal complexation. The shoulders at (410−413 nm) and (448−454 nm) are attributed to a curcumin → Mo charge transfer. The important feature of the spectra is the three weak absorption bands at 540, 585, and 600 nm, which are possibly due to the d−d transitions of Mo. The maximum absorption is due to the electronic dipole mediated $\pi-\pi^*$ type excitation of its extended conjugation system. Since there is electrostatic interaction between molybdenum and polar chromophores in curcumin molecule, this interaction tends to stabilize both the bonding electronic ground states and the π^*

DOI: 10.1021/acs.chemrestox.9b00135
Chem. Res. Toxicol. 2019, 32, 1599−1618

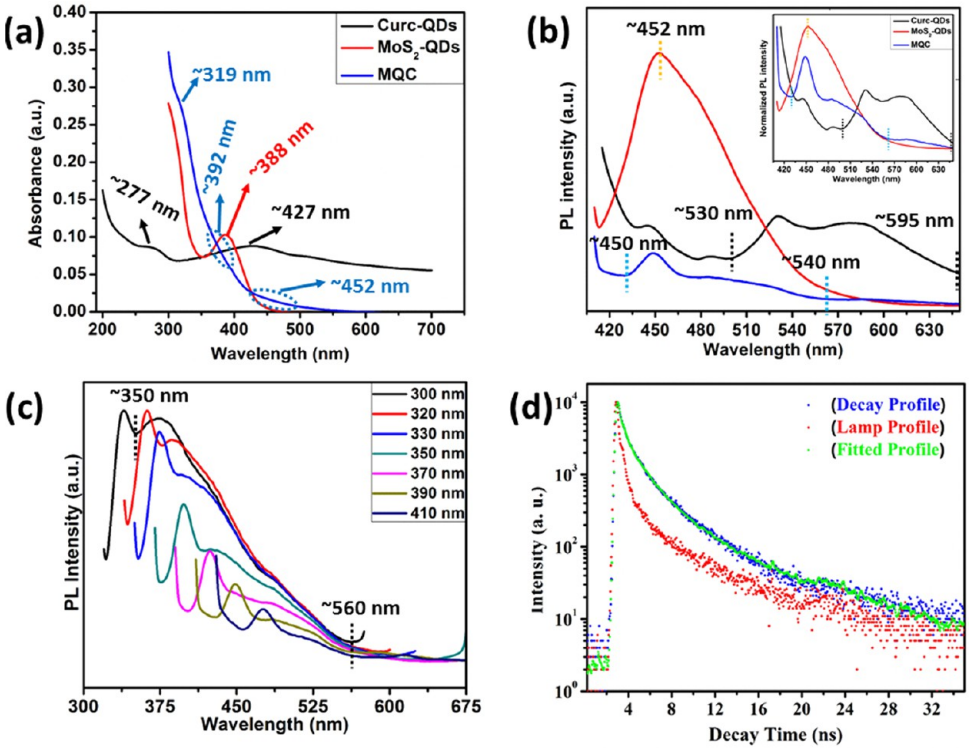

Figure 3. (a) UV−vis absorption spectra of curcumin, MoS_2-QDs, and MQC. (b) PL spectra of curcumin, MoS_2-QDs, and MQCs. Inset shows the normalized PL spectra of curcumin, MoS_2-QDs, and MQCs. (c) Excitation dependent PL spectra of MQC, and (d) TRPL spectra of MQC.

excited states. This interaction causes the n−π^* transition, which occurs at lower energy than the π−π^* transitions (i.e., decreased the band gap) to move to higher energy and π−π^* transition to move to lower energy. Thus, the π−π^* and n−π^* absorptions of curcumin move close to each other in case of MQCs.

PL spectra of curcumin, MoS_2-QDs and MQC are shown in Figure 3b for an excitation wavelength (λ_{ex}) ≈ 390 nm. The PL spectrum of curcumin shows a broad emission ranging from ∼530 to 595 nm, while MoS_2-QDs give comparatively a less broad PL band centered at ∼452 nm. This broad PL for curcumin may be due to the polydispersity of particles. PL spectrum of MQC is also broad ranging from ∼450 to 540 nm, possibly due to the combined effect of curcumin and MoS_2-QDs. Inset of Figure 3b shows the normalized PL spectra of curcumin, MoS_2-QDs, and MQC, respectively. From the inset of Figure 3b, it can be seen that the PL intensity of MoS_2-QDs is the maximum, while the curcumin has the minimum PL intensity. MQCs possess PL intensity in between MoS_2-QDs and curcumin. The photoluminescence (PL) and fluorescence of MQCs and MoS_2 were measured at the excitation wavelength of 390 nm in water and then compared in Figure 3b. At 390 nm excitation wavelength (see Figure 3c), MoS_2 showed a single less broad emission band at 452 nm, which originates possibly from the electron−hole recombination at the deep level caused by sulfur vacancy or molybdenum interstitial defects. Interestingly, in comparison to curcumin quantum dots, the emission of MQCs at 450 nm increased by ∼2-fold. Increased crystallinity and decreased surface defects may play key roles in this observation. Possibly, curcumin being the organic ligand has passivated the defects on MoS_2 surface, which act as visible PL centers, resulting in quenching the MoS_2 visible emission but improving the overall emission profile due to its own chromophore. The visible emission band of MQCs was found to be ≥10 nm red-shifted compared to that of MoS_2. MQCs gave an additional band at around 540 nm that was absent in MoS_2. The emission line at 540 nm may also be related to defect emission caused by curcumin. At excitation wavelength of 390 nm (Figure 3b), MoS_2 is not expected to have a good photoluminescence behavior due to poor light absorption in contrast to MQCs, which has a strong light absorption at this wavelength due to curcumin. Thus, the contribution of broad visible fluorescence of MQCs relative to MoS_2 is substantial at this excitation wavelength, and the emission is largely due to curcumin rather than MoS_2.

The Fourier transform infrared (FTIR)-attenuated total reflectance (ATR) spectroscopic investigation was performed to inspect the interaction(s) of curcumin with MoS_2 through the fingerprint vibrations of curcumin and MQCs as depicted in Supporting Information 2.

Excitation-dependent PL spectra of MQC are shown in Figure 3c. PL intensity of MQC is diminished for an excitation wavelength greater than ∼330 nm with red shifting in the maximum PL position. Red shift in the PL spectra of MQC may be attributed to the polydispersity of particles. TRPL spectrum of MQC is shown in Figure 3d. Decay curve has been fitted for the triexponential equation:

$$y = A\exp\left(-\frac{t}{\tau_1}\right) + B\exp\left(-\frac{t}{\tau_2}\right) + C\exp\left(-\frac{t}{\tau_3}\right) \quad (1)$$

The obtained data from the fitted graph are summed up in Supplementary Table S1.

Triexponential fitting of decay curve suggested the presence of three types of fluorescing species in MQC. Average decay time can be calculated using the following eq 2:

DOI: 10.1021/acs.chemrestox.9b00135
Chem. Res. Toxicol. 2019, 32, 1599−1618

Table 1. Minimum Inhibitory Concentration of MQCs *vis a vis* Vancomycin/Meropenem

bacterial isolate	MIC (μg/mL) for MQCs	MBC (μg/mL) for MQCs	MBIC (μg/mL) for MQCs	MIC (μg/mL) for Vancomycin[a]/Meropenem[b]	MBC (μg/mL) for Vancomycin[a]/Meropenem[b]
Klebsiella pneumoniae[b] (ATCC 700603)	<0.125	0.25	0.00625	0.5	1
Pseudomonas aeruginosa[b] (ATCC 25619)	0.25	0.5	0.00625	0.5	1
Staphylococcus aureus[a] (ATCC 29213)	<0.125	0.25	<0.00625	0.25	0.5
Klebsiella pneumoniae[b](Lab code: 10825/2018)	0.125	0.5	0.05	8	>16
Klebsiella pneumoniae[b] (Lab code: 1739/2018)	0.125	0.25	0.05	8	16
Pseudomonas aeruginosa[b] (Lab code: 2564/2018)	0.25	1	0.125	16	>16
Staphylococcus aureus[a] (Lab code: 1632/2018, MSSA)	<0.125	0.25	0.00625	2	4
Staphylococcus aureus[a] (Lab code: 699/2018, MRSA)	0.125	0.5	0.025	4	8

[a]Gram-positive isolates for which drug Vancomycin has been used. [b]Gram-negative isolates for which drug Meropenem has been used. MIC = Minimum inhibitory concentration, MBC = minimum bactericidal concentration, MBIC = minimum biofilm inhibitory concentration.

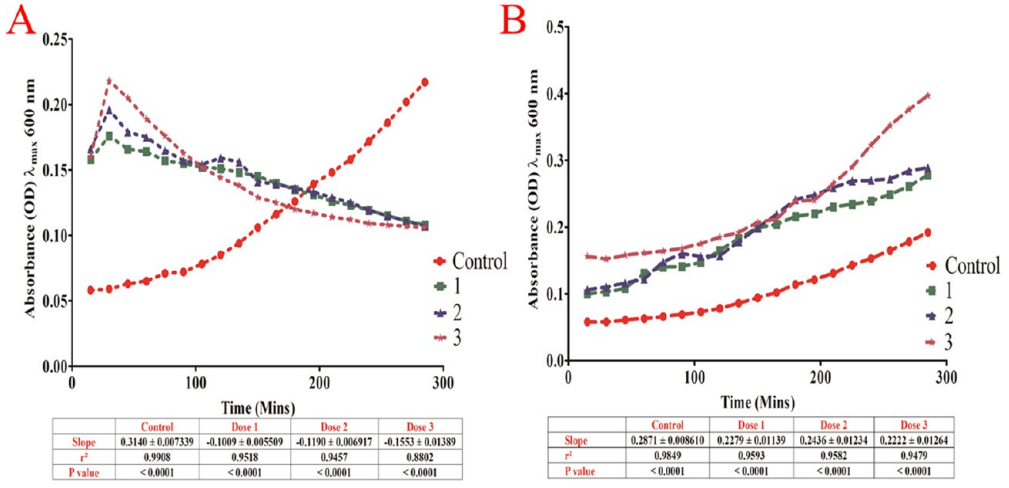

Figure 4. Growth rate analysis curve of (A) *K. pneumoniae* when treated with MQCs. (B) *K. pneumoniae* treated with MoS_2 QDs. In both cases, doses 1, 2, and 3 represented the exposure concentration of 0.0156, 0.0624, and 0.125 μg/mL.

$$< \tau_{av} > = \frac{B_1\tau_1^2 + B_2\tau_2^2 + B_3\tau_3^2}{B_1\tau_1 + B_2\tau_2 + B_3\tau_3} \quad (2)$$

Average decay time for triexponentially fitted MQC decay curve is calculated to be ~0.34 ns. We further calculated the quantum yield (QY) of MoS_2-QDs and MQC, which was found to be 0.0271 (Supporting Information 1; S2).

3.3. Minimum Inhibitory and Minimum Bactericidal Concentration (MIC and MBC) Determination. Antimicrobial activity of MQCs, and Meropenem against *Klebsiella* isolates and other mentioned bacteria were evaluated by determining MIC by broth microdilution assay. The MIC of MQCs against *Klebsiella* was 0.125 μg/mL, whereas MIC of Meropenem was found to be 8 μg/mL. This indicates that MQCs have potent antimicrobial activity against hv MDR *Klebsiella* isolates, which fostered significant killing of the bacteria under investigation, whereas the MoS_2 QDs and native curcumin were observed to be ineffective within the tested range. The MIC, MBC, and MBIC of MQCs against the tested pathogens are listed in Table 1.

3.4. Bacterial Growth Rate Analysis. Growth curves of the multidrug resistant isolate of *Klebsiella pneumoniae* were investigated with and without MQCs (Figure 4a). Their growth was inhibited by MQCs at a minimal concentration of 0.0156 μg/mL (dose 1) and at concentrations 0.125 μg/mL (dose 3), complete inhibition of the bacterial growth was manifested. MoS_2 QDs and the native curcumin were not found to be effective in the tested range, although they reduced the growth compared to the control (Figure 4b). These results depict the strong and immediate bactericidal activity of MQCs against the test bacteria even at significantly low concentrations.

3.5. Antibiofilm Assays. *3.5.1. Tissue Culture Plate Assay for Elucidation of Antibiofilm Potential of MQCs.* The MQCs mediated biofilm inhibition was dose-dependent against all the tested bacterial isolates. At the concentration 0.00625 μg/mL, MQCs was found to inhibit the biofilm formation by 73% but, no sooner, the concentration was escalated to 0.05 μg/mL, and then significant inhibition of 97% was observed in biofilms of *Klebsiella pneumoniae* (10825/2018) (Figure 5A), while at the same concentration, 84% inhibition was noted in *Klebsiella pneumoniae* (1739/2018) (Figure 5B). Interestingly, MoS_2 QDs were found to be poorly effective against the biofilms of tested isolates at the said concentration where merely 12% inhibition was realized. Remarkably, this inhibition is 13% lesser than the

DOI: 10.1021/acs.chemrestox.9b00135
Chem. Res. Toxicol. 2019, 32, 1599−1618

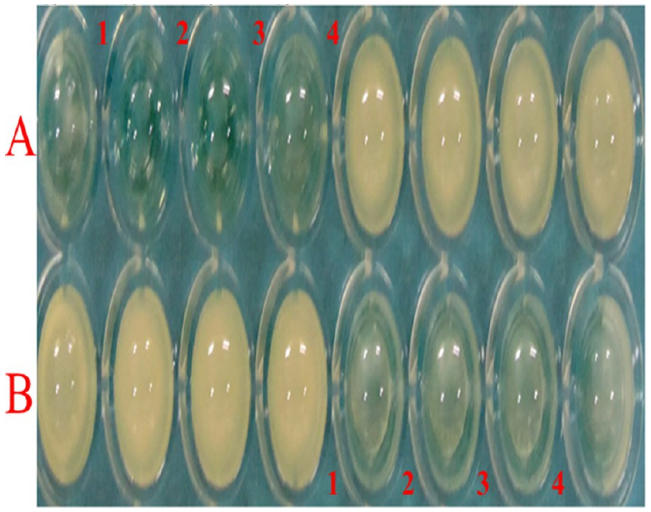

Figure 5. (A) Protein-rich biofilm of *Klebsiella pneumoniae* (10825/2018). (B) Sugar-rich biofilm of *Klebsiella pneumoniae* (1739/2018). The numerals 1−4 represent the wells containing the decreasing concentration of MQCs from 0.05, 0.025, 0.0125, 0.00625 μg/mL, respectively.

extent of inhibition manifested in case of protein-rich biofilm of *K. pneumoniae*.

3.5.2. Confocal Laser Scanning Microscopic Evaluation of Antibiofilm Potential of MQCs. The effects of MQCs on biofilms of high slime producing multidrug resistant clinical isolate (isolate no. 10825/2018) of *Klebsiella pneumoniae* were investigated by confocal microscopy. Seventy-two-hour old biofilm of the said isolate was then challenged with the MBIC concentration of MQCs (0.05 μg/mL) and then imaged by staining with the red fluorescent dye propidium iodide. Interestingly, the matured biofilm of the said bacterium showed an intense PI-staining, indicating the prevalence of dead cells after exposure to MQCs (Figure 6).

After administration of the minimal concentration of 0.05 μg/mL and incubation of 45 min, we observed only a few bacteria down the lanes, which were unable to conglomerate to form biofilm, indicating the complete inhibition of biofilm. This disintegration is accompanied by the dispersal (flow) of the biofilm debris. The results further show an obvious time-dependent disintegration of the biofilm matrix (Figure 6). This was evident by the observed rarefication of bacterial populations in panels L1, L2, and L3 of Figure 6, respectively. As we move down from panel A2 to C2, selective uptake of the drug (green fluorescence) by the bacteria can be noted. Further, the differential interference contrast (DIC) imaging (Lanes A1 to C1) also supports the confocal observations. By moving down the lane from L1 to L3, we may observe the progressive loss of cohesion (Lanes A1−C1 of Figure 6). The insets in panels L1−L3 are the enlarged view of bacterial populations post-treatment.

We found PI to be localized in the biofilm architecture. The MQCs are green autofluorescent molecules, and this property was, therefore, utilized for its localization in the biofilm (Figure 6,7). Surprisingly, we observed a clear colocalization of PI with MQCs in biofilm matrix. This colocalization was signaled by the presence of an intermediary yellow and even white fluorescence. To check the distribution of colocalization of PI with MQCs throughout the layers, we analyzed the different horizontal cross sections and found them frequently distributed across the biofilms as evident from yellow and white fluorescent specks/signals (Figure 7). This may be indicative of rather a peculiar phenomenon exhibited by MQCs, which might be simultaneously interacting with *Klebsiellar* biofilm-associated proteins (leading to biofilm disintegration). The fact that the dye PI binds to the nucleic acid of the dead cells, we, therefore, presume MQCs (due to curcumin) to pull PI toward itself, culminating in

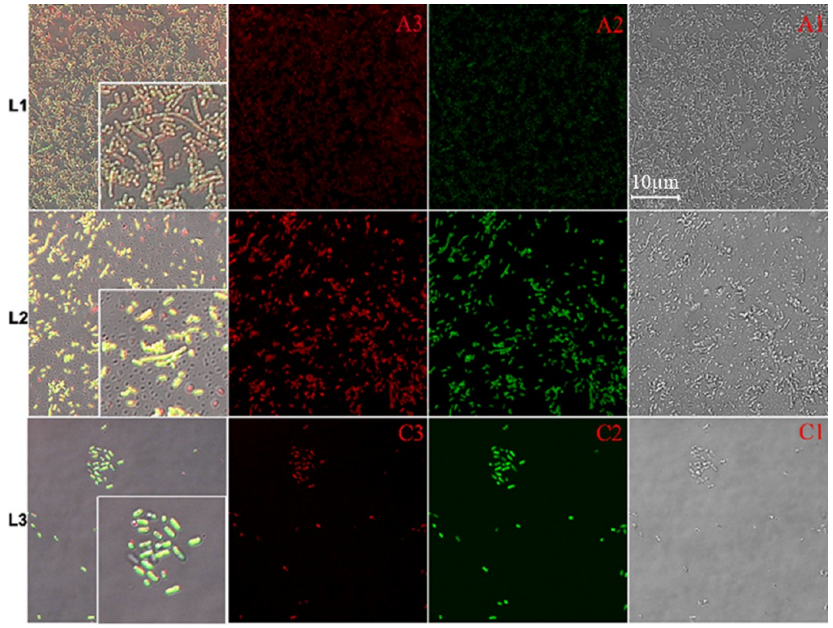

Figure 6. Static analysis of *K. pneumoniae* biofilm formation in the presence and absence of MQCs. (1) Time-dependent disintegration of biofilm matrix. *K. pneumoniae* biofilms were grown in BHI for 72 h in the presence of 0.05 μg/mL of MQCs at 37 °C for 45 min in chambered slides. Biofilms were stained and visualized using propidium iodide (PI) to stain dead cells red and examined by confocal microscopy. The presence of only a few bacteria down the lanes L1−L3 reveals the inability of *Klebsiella* isolate to form biofilm, indicating the biofilm inhibitory potential of the MQCs.

DOI: 10.1021/acs.chemrestox.9b00135
Chem. Res. Toxicol. 2019, 32, 1599−1618

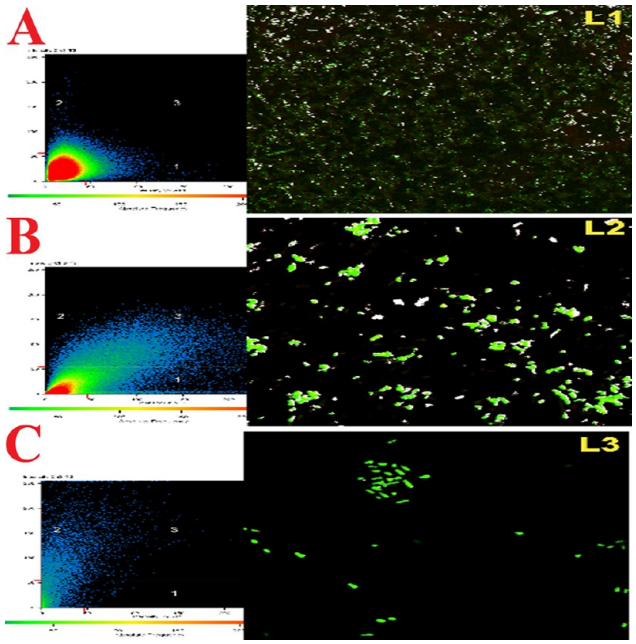

Figure 7. Colocalization maps of MQCs with biofilm matrix components obtained from different horizontal sections of the biofilm. The high prevalence of intense yellow and white fluorescence (L1, L2, and L3) can be seen with noticeable stability of yellow curve in panels A−C exhibiting stable colocalizations or interactions between MQCs and the biofilm matrix material.

colocalization (Figure 7). This signaled some other targets of MQCs beside the matrix structuring proteins.

Thereafter, we assessed the nature and stability of PI−MQCs complex by colocalization maps obtained from different horizontal sections of the biofilm. One can see the intense yellow and even white fluorescence in excess in the panel L1 of Figure 7. It is noticeable that the shift of yellow curve (Figure 7A) exhibits linearity with respect to the red and green signals that indicate significantly stable colocalizations or interactions between drug and the genetic material of the bacteria. This observed interaction between the dyes can be seen throughout the biofilm layers (Panels L1−L3, Figure 7).

Of note, in Figure 8A, we can see the precise overview of drug colocalization. The drug seems to foster the rupture of the plasma membrane, which ultimately leads to the ooze out of cytosolic content from the bacteria as revealed by the red signals of PI coming out of the cell. In another set of experiments, we looked for the transverse sections of biofilm (thickness-wise evaluation). For this, we used Concanavalin A, labeled with tetramethyl-rhodamine isothiocyanate (TRITC), which selectively binds with the sugars of the biofilm matrix. Figure 8B clearly depicts the percolation of the MQCs to the benthic regions of the *Klebsiellar* biofilm. Panel D′ is the control lane that was stained by Concanavalin A, labeled with tetramethyl-rhodamine isothiocyanate (TRITC). We can see as we move from panels A′ to C′, MQCs are not just percolating inside the matrix but they are also disintegrating the biofilm architecture leading to the rarefication of bacteria as indicated by the significantly reduced number of bacterial cells in the field. Panels A to C of Figure 8B are the DIC images of the vertical sections of the same regions of which we studied the transverse sections.

Therefore, it can easily be inferred that the reduction in particle size to 13 nm be the reason for better percolation to the bottom regions of the biofilm, high-affinity interaction with the biofilm matrix, and relatively higher uptake by the bacterial cells.

3.6. Changes in Membrane Dynamics. We investigated the hypothesized MQCs mediated alterations in membrane dynamics by using DPH assay. DPH intercalates in the membrane lipid bilayer via interactions with acylated lipids and then exhibits fluorescence.[21] However, in the case of impaired membrane integrity, the lipid dynamics is altered, and consequently, insertion of DPH into the membrane does not take place, culminating in the decreased fluorescence intensity. This was assessed by using steady-state fluorimetry assay (Figure 9A) wherein the untreated control exhibited strong fluorescence intensity (fluorescence unit ~10^2 arbitrary units (a.u.) was set as threshold fluorescence). The incubation of *Klebsiella pneumoniae* with MIC concentration of MQCs for 120 min showed a significant decrease in DPH fluorescence intensity in comparison to the untreated control. As depicted in Figure 9A, the DPH intensity was 96.00 ± 2.646 au for untreated *Klebsiella pneumoniae* cells. Interestingly, upon exposure to the 0.5 μg/mL concentration of MQCs for 120 min, the DPH fluorescence intensity reduced to 57.33 ± 5.508 au. However, upon treatment with MoS_2 QDs, the fluorescence was found to be 82.33 ± 3.055 au. Figure 9A unveils the significant decrease of 51.731% in DPH fluorescence that at exposure to MIC in comparison to the

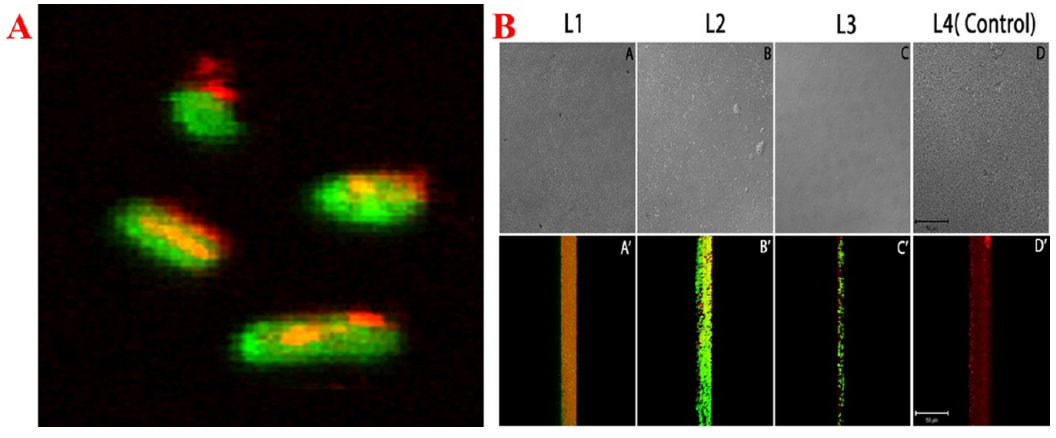

Figure 8. (A) Ooze out of propidium iodide (PI) indicating the rupture of the plasma membrane. (B) The confocal micrographs showing transverse sections of Klebsiellar biofilm stained with Concanavalin A, labeled with tetramethyl-rhodamine isothiocyanate (TRITC) revealing the trickling of MQCs down the matrix, which fostered the disintegration of the biofilm matrix.

DOI: 10.1021/acs.chemrestox.9b00135
Chem. Res. Toxicol. 2019, 32, 1599−1618

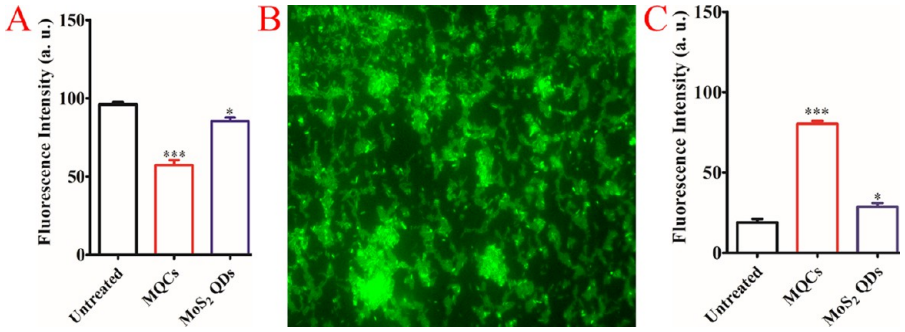

Figure 9. (A) Steady-state 1,6-diphenyl-1,3,5-hexatriene based fluorimetry assay. The incubation of *Klebsiella pneumoniae* with MIC concentration of MQCs for 120 min showed a significant decrease in DPH fluorescence intensity (shown in red) in comparison to the untreated control (shown in black). (B) Sytox Green staining of MDR *Klebsiella pneumoniae* after MQCs treatment. The green emission wavelength represents Sytox Green stained cells with fluorescence microscopy. At MIC concentration of MQCs, the clear uptake of Sytox Green symbolizes membrane perturbation. Treatment was for 120 min. (C) Steady-state 3,3′-dipropylthiadicarbocyanine iodide based fluorimetry assay. The fluorescence intensity is function of leaked [$DiSC_3$−5]. Therefore, the untreated control cells (shown in black) produce a low signal intensity, whereas the depolarized cells (shown in red) produce a high signal intensity.

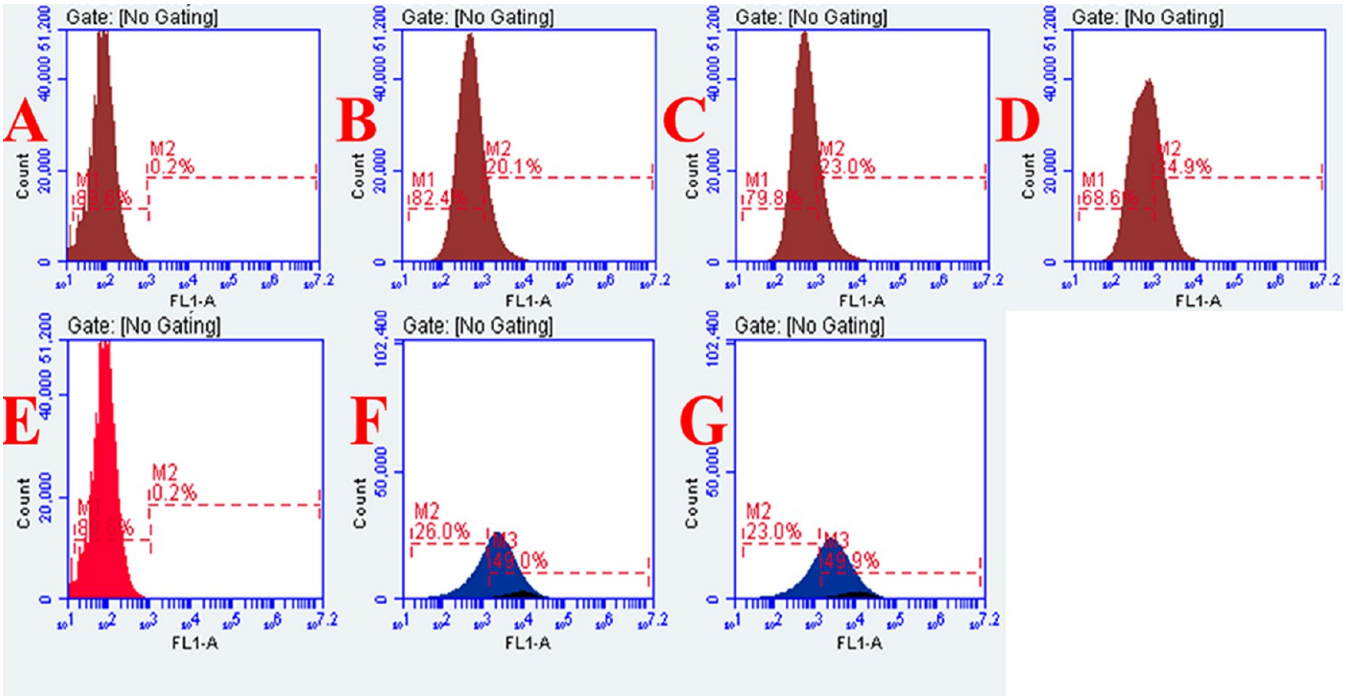

Figure 10. Flow cytometry analyses of *Klebsiella pneumoniae* with DPH to explore the changes in its membrane dynamics in the groups treated with two discrete quantum dots. The symbols, pattern, and colors used here remained the same for every panel. Total 10 000 000 cells were taken into account for each analysis. (A) Histograms of untreated logarithmic *Klebsiella* cells labeled with DPH. (B) Histograms of MoS_2 QDs (2 mg/mL) treated *Klebsiella* isolates labeled with DPH. The panels show the increase in cell population (20.1%) that had taken up DPH, which shifted right, indicating the damage to the cell membrane. (C) Histograms of native curcumin (2 mg/mL) treated *Klebsiella* isolates labeled with DPH. The panel shows the increase in cell population (23%) that had taken up DPH that shifted right, indicating the damage to the cell membrane. (D) Histograms of native curcumin (8 mg/mL) treated *Klebsiella* isolates labeled with DPH. The panels show the increase in cell population (~35%) that had taken up DPH, which shifted right, indicating the damage to the cell membrane. (E) Histograms of untreated logarithmic *Klebsiella* cells labeled with DPH. (F) Histograms of MQCs (0.5x MIC) treated *Klebsiella* isolates labeled with DPH. The panels show the significant increase in cell population (40%) that had taken up DPH indicating increased alteration in membrane lipids. The panel shows that the majority of cell population had shifted right with the intensity significantly lower compared to the untreated control, which depicts the significant alteration in permeability and the lipid portion of the membrane by the MQCs treatment. (G) Histograms of MQCs (MIC) treated *Klebsiella* isolates labeled with DPH. The panels show the significant increase in cell population (49%) that had taken up DPH indicating increased alteration in membrane lipids. The panel shows that the majority of cell population had shifted right with the intensity significantly lower compared to the untreated control, which depicts the significant alteration in permeability and the lipid portion of the membrane by the MQCs treatment.

untreated control, which indicates the altered dynamics of membrane lipids.

We noted the same vogue of alteration in membrane dynamics after the flow cytometry assessment. As shown in Figure 10, we confirmed that MQCs, at minimum inhibitory concentration, fostered a substantial shift in the DPH fluorescence (and hence diminished counts, Figure 10g), which indicated the alterations in membrane lipids. The DPH positive *Klebsiella* cells constituted 89.6 ± 2.1% of the untreated sample, whereas MoS_2 QDs and curcumin treated cells were

DOI: 10.1021/acs.chemrestox.9b00135
Chem. Res. Toxicol. 2019, 32, 1599−1618

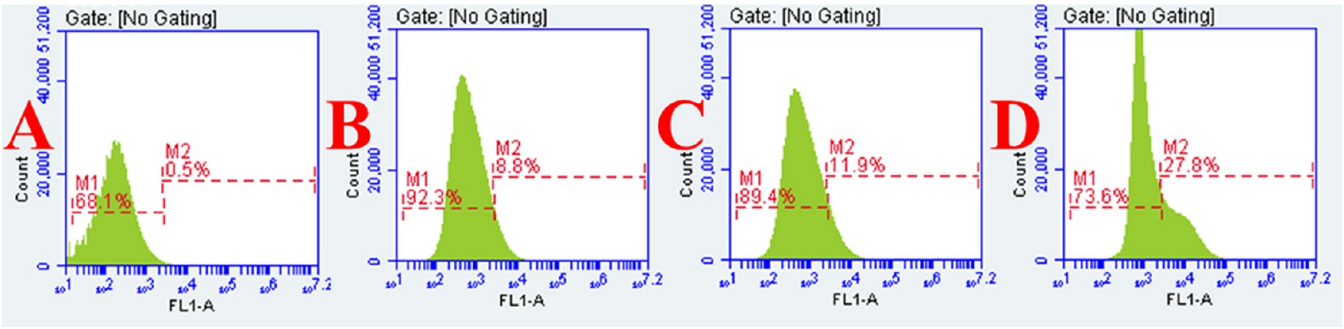

Figure 11. Flow cytometry analysis of *Klebsiella pneumoniae* with membrane potential-sensitive dye, $DiSC_3$−5, to explore the alterations in its membrane dynamics in the groups treated with two discrete quantum dots. Total 10 000 000 cells were taken into account for each analysis. (A) Histogram of untreated logarithmic phase *Klebsiella* cells labeled with $DiSC_3$−5. (B) Histograms of native curcumin (8 mg/mL) treated *Klebsiella* isolates labeled with $DiSC_3$−5. The panels show the increase in cell population (8.8%) that had taken up DiSC3−5 with the same peak position with increased intensity, which signals the membrane depolarization. (C) Histograms of MoS_2 QDs treated *Klebsiella* isolates labeled with $DiSC_3$−5. The panels show the increase in cell population (11.9%) that had taken up $DiSC_3$−5 but the peak position remained the same with increased intensity, which denotes the membrane depolarization. (D) Histograms of MQCs treated *Klebsiella* isolates labeled with $DiSC_3$−5. The panel demonstrates the increase in cell population (27.8%) that had taken up $DiSC_3$−5. Note that the greater part of cell population shifted right with the intensity significantly higher compared to the untreated control and the other treated groups, which depicts the significant alteration in membrane potential leading to the depolarization of the by the membrane post MQCs treatment.

20.1 ± 1.45% and 34.9 ± 2.1%. However, the DPH positive MQCs treated cells constituted merely 49.9 ± 0.72%. Curcumin at the concentration 2 mg/mL has led to the more pronounced membrane alterations. However, MQCs have fostered membrane alterations more prominently at minimal concentration of 0.5 μg/mL. The results indicate possible alteration caused by clustering of anionic lipids/proteins with "Mo" having multiple positive charges that prevent the interaction of lipids/proteins with other cell membrane components or forms phase boundary defects between the clustered lipids and the bulk of the membrane. Another possibility is the interaction of curcumin part with proteins that maintain the outer membrane lipid asymmetry and integrity like "Mla" macro molecular system.

3.7. Membrane Permeabilization Assay. We used Sytox Green (Molecular Probes, Invitrogen), a nucleic acid staining dye that can only penetrate a compromised membrane, to determine whether the MQCs caused membrane permeabilization employing fluorescent microscopy as well as UV-spectroscopy (Figure 9B). The fluorescent microscopy gave a more detailed picture of perturbation of membrane permeability during exposure to MQCs.[22] Using Sytox Green as a nucleic acid stain, its presence can be seen unequivocally at or around the cell membrane and throughout the cytoplasm of the *Klebsiella* rods (Figure 9B). Similarly, the presence of red signals of PI as depicted in confocal micrographs (Figure 8A) shows membrane breaching. Thus, an appealing hypothesis is that MQCs foster cell deaths by localizing on cell surfaces and hence increasing the membrane permeabilization will lead to impaired bacterial survival and conglomeration necessary for biofilm development.

We delineated the bactericidal mechanism of MQCs by interpreting the findings of three different tools, namely spectrofluorimetry, fluorescent microscopy, and flow cytometry together. Various studies endorse the influence of curcumin on structurally unrelated membrane proteins and lipid domains across numerous signaling pathways at nano/micromolar concentrations; therefore, we conjectured that curcumin acts on membranes indirectly by altering its physical properties rather than by the direct binding. Hydrophobic domains help integral proteins glue up with the hydrophobic lipid core of the membrane. Therefore, a perfect match between the length of the transmembrane protein segments and the hydrophobic thickness of the bilayer is indispensable to maintain their conformational equilibria. The elastic modulus is a prominent determinant of membrane distortion. Integral membrane proteins have much higher elastic moduli compared to the membrane as a whole. Therefore, membranes are innately disposed to deformation to match the membrane hydrophobicity (lipid domains) and anchoring interactions of the integral proteins. The maintenance of this deformation needs energetic forfeit. This situation is well utilized in our current study design. Integration of MoS_2 modified curcumin QDs may alter its hydrophobic width. A recent report by Ingolfsson et al. proves this by measuring the effects of curcumin on the activity of gramicidin channels of varying lengths and amino acid sequences in dioleoylphosphatidylcholine (DOPC) membranes. Dimerization of gramicidin in membrane is the prerequisite for the formation of an active gramicidin channel, which in turn is dependent on the deformation of the bilayer. They found that the addition of curcumin to the system has increased both gramicidin channel lifetimes and their appearance rates. From here, one can clearly insinuate that curcumin decreases the energetic penalty of the bilayer deformations.[28] Recently, Alsop et al. has reported that curcumin can bind to the membranes in two modes: the surface associated mode in the carpet model and the transmembrane mode in insertion model.[29] Taking account of our previous studies and the above-mentioned studies, we looked for the solution to the menace of multidrug resistant isolates by altering their membrane dynamics by alterations in the fluidity of the lipid bilayer.

3.8. Membrane Depolarization Assay. The membrane potential of the normal cell remains unperturbed unless it undergoes any membranous change, and when this potential gets disturbed, the membrane depolarizes. To explore if MQCs resulted in membrane depolarization, we performed steady-state fluorimetry and flow cytometry investigations of multidrug resistant *Klebsiella pneumoniae* cells using the membrane potential-sensitive dye, $DiSC_3$-5. The fluorescence of the dye decreases as it partitions into the surface of polarized cells, however, membrane depolarization precludes its partitioning, and hence the dye is released into the growth medium. The fluorescence intensity is proportional to the amount of $DiSC_3$-5

DOI: 10.1021/acs.chemrestox.9b00135
Chem. Res. Toxicol. 2019, 32, 1599−1618

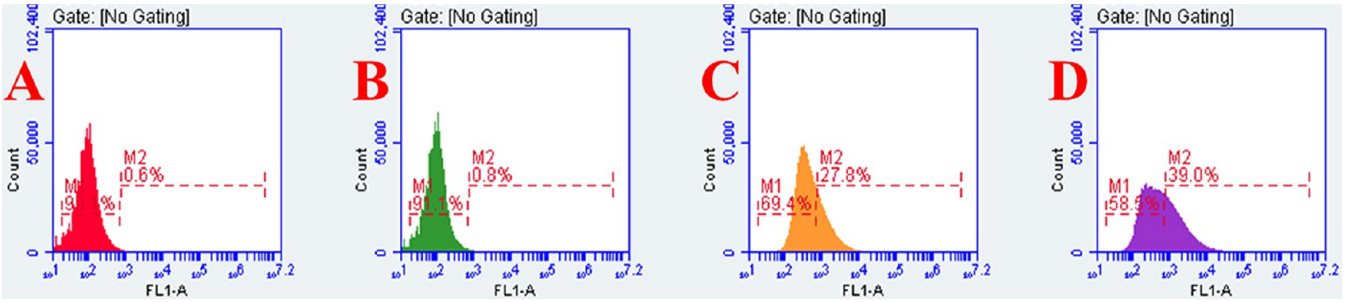

Figure 12. Flow cytometry analysis of *Klebsiella pneumoniae* with ROS-sensitive dye, DCFDA to explore the post treatment ROS status in the groups treated with MoS_2 QDs, curcumin, and MQCs. Total 10 000 000 cells were taken into account for each analysis. (A) Histogram of untreated logarithmic phase *Klebsiella* cells labeled with DCFDA. (B) Histograms of MQCs treated *Klebsiella* isolates labeled with DCFDA. The panels show the minimal increase in cell population (0.8%) that had taken up DCFDA indicating minimal ROS generation. (C) Histograms of native curcumin treated *Klebsiella* isolates labeled with DCFDA. The panels show the increase in cell population (27.8%) that had taken up DCFDA, which denotes the ROS generation. (D) Histograms of MoS_2 QDs treated *Klebsiella* isolates labeled with DCFDA. The panel demonstrates the increase in cell population (39%) that had taken up DCFDA. Note that the greater part of cell population shifted right which reveal the significant production of ROS post MQCs treatment.

leaked.[23] Therefore, the untreated control cells produce a low signal intensity, whereas the depolarized cells produce a high signal intensity. In the current study, the untreated control exhibited negligible fluorescence intensity (fluorescence unit $<10^2$ arbitrary units (a.u.) was set as threshold fluorescence). As shown in Figure 9C, the addition of 0.5 μg/mL MQCs resulted in a significant increase in fluorescence, which indicated the MQCs mediated depolarization of the cell membrane. In comparison to the untreated cells, the cells depolarized by MQCs accounted for 58.81% of total cells, while MoS_2 QDs accounted for 17.57% of the total cells. As depicted in Figure 9C, the $DiSC_3$-5 intensity was 18.67 $\pm$ 2.082 au for untreated *Klebsiella pneumoniae* cells. Interestingly, upon exposure to the said MIC concentration of MQCs for 120 min, the $DiSC_3$-5 fluorescence intensity intensified to 82.00 $\pm$ 4.583 au. However, upon treatment with MoS_2 QDs, the fluorescence was found to be 40.00 $\pm$ 6.557 au (Figure 9C).

Flow cytometry evaluation further revealed the increase in the population (0.5% to 27.8%) and intensity of fluorescence of the depolarized cells after MQCs treatment for 120 min in comparison to the untreated cells (Figure 11). These results clearly demonstrate that MQCs bring about membrane depolarization. In contrast, curcumin and MoS_2 QDs have fostered membrane depolarization in only 8.8% and 11.9% of the cell population (Figure 11B,C). The growth rate analysis along with cell viability assay reveals the decrease in growth rate as well as in cell viability after MQCs treatment. During the same period, the changes in membrane potential establish some temporal correlation between membrane depolarization and stunted growth rate with reduced viability. The data further suggested that the entire population of *Klebsiella* was progressively depolarized, which resulted in a less wide and bimodal distribution (Figure 11d). This distribution suggests that membrane potential in individual bacteria is lost gradually rather than instantaneously.

The previously mentioned results along with the increased concentration of Sytox-green and PI in- and outside the bacterial cells, respectively (in fluorescent and confocal micrographs), clearly indicate that membrane depolarization was the resultant of the cumulative effect of membrane dynamics alterations and the rupture/lysis of the cell membrane. Therefore, these results are in consonance with the results obtained by CLSM and indicate that the MQCs are possibly fostering membrane permeabilization by the alteration of the lipid domains that finally results in membrane depolarization, which eventually kills the bacteria.

3.9. Reactive Oxygen Species Generation. The bacterial cells exposed to the MIC concentrations of MQCs, curcumin, and MoS_2 QDs were evaluated for ROS generation by probing with 2′,7′-dichlorfluorescein-diacetate (DCFH-DA) using flow cytometry. We observed significant differences in the ROS generation profile of the three discrete compounds used herein as evident from the increased intensity/count in the DCF fluorescence in curcumin and MoS_2 QDs treated cells compared to those of MQCs (Figure 12). MoS_2 QD treated cells exhibited a significant increase in the DCF fluorescence compared to the MQCs treated and curcumin cells (Figure 12B–D). The population shift was significant (39%) in MoS_2 QDs treated group. However, no significant increase in the fluorescence was perceived when the cells were treated with MQCs. The population, which exhibited ROS generation, was only 0.8%. This showed that MQCs fostered significantly low ROS generation in comparison to the MoS_2 QDs and curcumin.

The results obtained are in agreement with the recent report, which suggests the deep insertion of curcumin in the membrane in a transbilayer orientation resulting in negative curvature in the bilayer. The negative curvature increases the permeabilizing activity resulting in the cell death.[30] In all, the present study investigates the loss of integrity of the bacterial membrane due to MQCs exposure, using three different fluorescent-based assays utilizing DPH, Sytox Green, and $DiSC_3$-5. Our results portray that upon MQCs exposure there occurs alterations in membrane dynamics of the lipid bilayer, which fosters depolarization and increases the permeability of the membrane finally culminating in the cellular deaths without significant ROS generation. Data of killing, membrane dynamics study, membrane permeabilization study along with depolarization study establish that a 2 h exposure to MIC concentration of MQCs causes 100% killing with 10^6 CFU/mL bacterial density.

3.10. *In Silico* Study. In general among Gram-negative bacteria three major systems have been defined to maintain the outer membrane lipid asymmetry and integrity, that is, the phospholipase A2 PldA, the lipopolysaccharide palmitoyl transferase PagP, and the Mla (maintenance of outer membrane lipid asymmetry) macro molecular system.[31,32] Among these three, only the Mla system is reported to maintain the membrane asymmetry directly via phospholipid extraction, while PldA and PagP both generate lysophospholipids in the outer leaflet that

DOI: 10.1021/acs.chemrestox.9b00135
Chem. Res. Toxicol. 2019, 32, 1599−1618

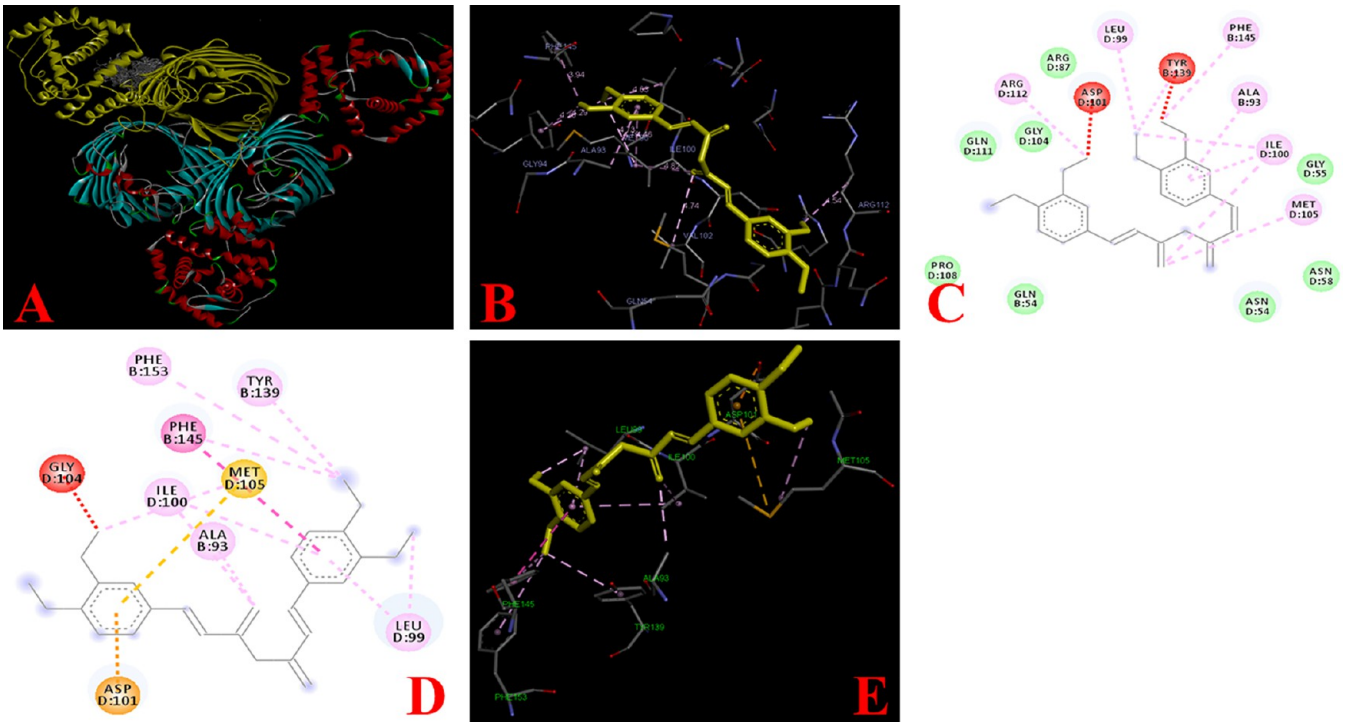

Figure 13. Region of precision controlling with (A) center grid value of −35.046, 58.825, and −40.650 (x, y, and z) of docking consist of B and D chain of Mla system. (B) 3D diagram of the AutoDock interaction in B and D chain. (C) 2D diagram of the AutoDock interaction in B and D chain. (D) 2D diagram of the Vina interaction in B and D chain. (E) 3D diagram of the Vina interaction in B and D chain.

Table 2. Summary of *in Silico* Docking Result

Sl no.	controlling center grid value (x, y, and z)	chain contains	binding affinity (kcal/mol)		amino acids
			AutoDock	Vina	
1	−35.046, 58.825, −40.650	B and D	−7.12	−7.3	ALA93, PHE153, TYR139, LEU99, MET105, ILE 100, ARG112
2	−20.046, 15.925, −80.138	A, C, and E	−6.89	−8.5	ILE100, MET96, TYR139, LEU155, PHE145
3	−25.046, 78.925, −70.138	B	−6.13	−6.4	ARG 271, TYR227, TYR304, VAL114

still requires removal. The Mla system consists of the inner membrane ABC transporter MlaBDEF, the periplasmic protein MlaC, and the outer membrane lipoprotein MlaA.[33−35] MlaA is documented as a major virulence factor in various bacterial pathogens.[36−38] For the evaluation of the bacteria membrane rupture due to alterations in membrane dynamics and depolarization, we took MlaA protein system (PDB ID: 5NUP) of *Klebsiella pneumoniae* into account for the docking study (Figure 13).[39]

Being lipid macromolecular system, the predominant interaction in the study was found to be hydrophobic between the macromolecule and the ligand. To identify the possible region of interaction, each portion of the MlaA and OmpF (outer membrane protein F) trimeric complex system was subjected to docking. The Mla system is a trimer of OmpF positioned at the center forming a porin like structure referred as A, B, and C chain. On the other hand, each monomer of OmpF forms a dimeric complex with each MlaA system, the ring shaped predominant α-helical structure forming hydrophobic surface, which has been referred to as D, E, and F chain, respectively. Among them, the molecule toward the region of precision controlling center grid value of −35.046, 58.825, −40.650 (x, y, and z) with grid set 60 × 60 × 60 of the macromolecule, consist of B and D chain, that is, region in between the one dimeric complex of the MlaA−OmpF had shown highest affinity (Figure 13A). In AutoDock, the affinity value was found to be −7.12 kcal/mol, while in Vina, the affinity value came out to be −7.3 kcal/mol. In docking, the hydrophobic interaction with curcumin was exhibited by ALA93, PHE153, and TYR139 of OmpF monomer and LEU99, MET105, ILE 100, and ARG112 of MlaA system (Figure 13B−E). The results of the present study have been summed up in Table 2.

3.11. *In Vitro* Evaluation of Cytotoxicity. *3.11.1. Hemocompatibility Analysis.* Erythrocytes membrane stability is a reliable indicator of the compatibility of any drug for systemic use.[7,40] As evidenced by the results (Figure 14A), the percent viability was 95.3, 93.8, 89.5, 87.3, and 84.7% in the presence of MQCs at the much higher concentrations 64, 128, 256, 512, 1024 μg/mL, respectively, compared to the MIC, while MoS_2 QDs have fostered RBC rupture in a dose-dependent manner. Of note, MoS_2 QDs mediated rupture was perceived even at the minimal concentration of 8 μg/mL, and when the concentration was raised to 1024 μg/mL, percent viability of RBCs was found to be reduced to <20%.

3.11.2. LDH Assay. The MQCs mediated structural damage (toxicity) to the cell was further investigated using LDH assay to assess its toxicity.[7,27] Table 3 shows the LDH activity (in terms of mean absorbance) in percentage after 48 h exposure of the SiHa cells to the MQCs and MoS_2 QDs. At any given time, SiHa cells incubated with MQCs at various concentrations (32, 64,

DOI: 10.1021/acs.chemrestox.9b00135
Chem. Res. Toxicol. 2019, 32, 1599−1618

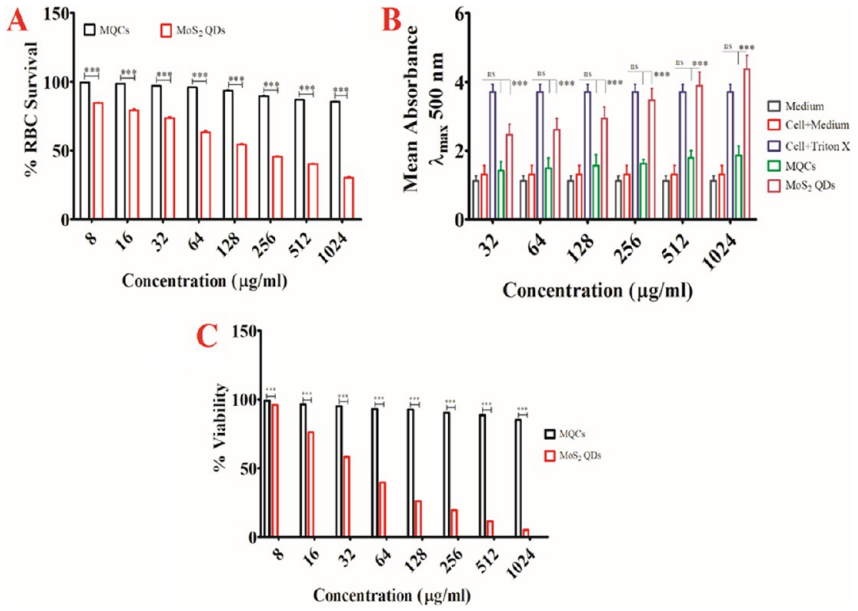

Figure 14. Biocompatibility evaluation. (A) Hemo-compatibility evaluation of MQCs vis a vis MoS_2 QDs. The plot corresponds the percent viability of 99.59 ± 0.0987, 98.71 ± 0.624, 97.10 ± 0.375, 95.89 ± 0.248, 93.66 ± 0.644, 89.69 ± 0.712, 86.93 ± 0.766, and 85.51 ± 0.921 in the presence of MQCs at concentrations 8, 16, 32, 64, 128, 256, 512, 1024 μg/mL, respectively, showing minimal toxicity over RBCs, while its counterpart MoS_2 QDs had shown significant hemolysis at all concentrations. (B) Lactate dehydrogenase assay for cytotoxicity evaluation. The plot shows relative enzyme activity in terms of absorbance. The experiment had three controls parameters, 1. The medium alone, 2. Cells with the medium, 3. The cells treated with 2% Triton X, 100. Minimal LDH activity was found in the group treated with MQCs indicating negligible cell lysis, while the MoS_2 QDs treated group had shown dose-dependent cell lysis with maximum LDH activity at the concentration of 1024 μg/mL. (C) Cell viability analysis using Sulforhodamine B (SRB) assay. The results of SRB assay corroborate well with the aforementioned assays. The cellular viability of SiHa cells remained intact even at highest treated concentration of MQCs, while its counterpart MoS_2 had shown pronounced killing (<20%) at 1024 μg/mL concentration.

Table 3. Lactate Dehydrogenase Cytotoxicity Assay against SiHa Cells

medium absorbance (λ_{max} 500)	cell + medium absorbance (λ_{max} 500)	cell + 2% Triton X 100 absorbance (λ_{max} 500)	concentration (μM)	MQCs treated cells absorbance (λ_{max} 500)	MoS_2 QDs treated cells absorbance (λ_{max} 500)	% cytotoxicity by MoS_2 QDs
1.126 ± 0.103	1.322 ± 0.294	4.012 ± 0.323	32	1.410 ± 0.271	2.467 ± 0.304	0.706
			64	1.490 ± 0.292	2.612 ± 0.325	6.096
			128	1.570 ± 0.315	2.935 ± 0.334	18.104
			256	1.630 ± 0.117	3.471 ± 0.340	38.031
			512	1.790 ± 0.208	3.901 ± 0.398	54.014
			1024	1.860 ± 0.277	4.379 ± 0.395	71.784

128, 256, 512, 1024 μg/mL) showed nonobservable minimal LDH activity than the group inoculated with MoS_2 QDs in the same concentration range, which demonstrated that MoS_2 QDs fostered cell leakage in a dose-dependent manner (Figure 14B). At the concentration of 1024 μg/mL, around 72% cytotoxicity was noted in the MoS_2 QDs treated cells, while on the same concentration, no leakage was noted in MQCs treated cells. This indicates biocompatibility of MQCs, which was in consonance with the phase contrast micrographs.

The formula used for % cytotoxicity calculation is as follows: % Cytotoxicity = (Mean Absorbance of Treated Cells − Absorbance of Medium − Absorbance of Cell and Medium)/(Absorbance of Triton X Treated Cell − Absorbance of Cell and Medium) × 100.

3.11.3. Sulforhodamine B Assay. The *in vitro* cell growth inhibition (viability) in the presence of MQCs was evaluated by SRB assay (Figure 14C). This killing potential of the drug can be reckoned effectively by this method.[26] Incubation of SiHa cells with MQCs did not influence cell viability in the tested range (2−1024 μg/mL), which can be inferred from the fact that upon exposure to 2 μg/mL MQCs, cell viability was around 99%, which remained 91.07% (almost unchanged) when exposed to 1024 μg/mL. Unlike MQCs, the MoS_2 QDs affected the cell viability in a concentration-dependent manner. For instance, at 2 μg/mL concentration, around 96% cell viability was noted but as the concentration was raised to 1024 μg/mL; cell viability was reduced to <20%. The viability and proliferation rate of SiHa cells was directly proportional to the optical density of the reaction product from the SRB working solution with live cells. As seen, clearly in Figure 14, after 72 h, the viability remained unaltered compared to the MoS_2 treated cells, indicating its improved biocompatibility.

Although QDs have promising activities as a therapeutic agent, a detailed biocompatibility evaluation is lacking in the literature. Therefore, we evaluated its biocompatibility of MQCs using SiHa cells after exposure for 72 h by phase contrast, SRB-assay, and LDH-assay. Images reveal unaltered proliferation over the time with more pronounced polygonal morphology that suggests restoration of SiHa functionality (Figure 15).

3.12. *In Vivo* Evaluation of Cytotoxicity. *3.12.1. Body and Organ Weights.* Body weights of all rats were recorded before and after MQCs administration in 2 days interval for 14

DOI: 10.1021/acs.chemrestox.9b00135
Chem. Res. Toxicol. 2019, 32, 1599−1618

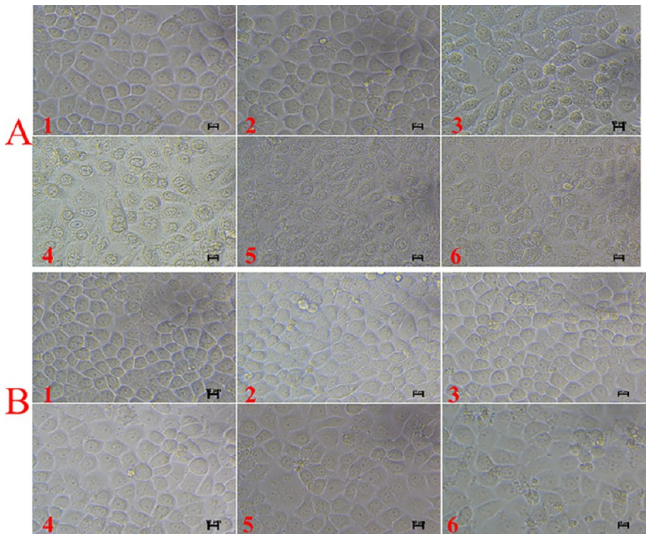

Figure 15. Evaluation of morphology of the SiHa cells post-treatment. (A) MoS_2 QDs treated group. Panel 1 represents the untreated control while panels 2−6 represent treated populations with concentrations 64, 128, 256, 512, and 1024 μg/mL. As evident from the micrographs, at mere concentration of 128 μg/mL, the morphological alterations were manifested and plasma membrane of the SiHa cells started distorting. As the concentration was escalated to 256 μg/mL and above, evident necrosis was seen. (B) MQCs treated group. Panel 1 represents the untreated control while panels 2−6 represent treated populations with concentrations 64, 128, 256, 512, and 1024 μg/mL. Remarkably, even at highest exposed MQCs concentration, no morphological alterations were observed.

days. Among all groups, no significant variation in the body weights of rats was observed. However, the MoS_2 QDs treated group has shown loss of weight (Supporting Information 3; S3). In addition, the vital organs such as liver, kidney, and spleen from MQCs administered rats showed no significant weight differences compared to the control groups. However, the MoS_2 QDs treated group has shown loss of weight of all vital organs. The organ to body mass ratio index, which confirmed the same, further certified this loss (Supporting Information 3; S4).

3.12.2. Biochemical Evaluation of Serum. Toxicity testing of MQC has been done on rats, and different cellular parameters were assessed in blood serum as listed in Supporting Information 3. No significant change in serum glucose concentration was found among different groups. However, a significant reduction in the level of Hb in MoS_2 QDs treated group (group II) was noted. Unlike group II, no significant changes were observed in Hb concentration among MQC treated test groups as compared to the normal group. We further evaluated the levels of alanine aminotransferase (ALT/GPT), and aspartate aminotransferase (AST/GOT) in MQCs treated groups *vis a vis* MoS_2 QDs treated groups with respect to the untreated control group. Interestingly, no significant increase in the ALT/GPT and AST/GOT activities in any MQCs treated groups (group III−VI) was observed; however, the MoS_2 QDs treated group II had shown the marked increase in ALT and AST activities. Similarly, we documented significantly increased concentration of serum urea and creatinine ($p \leq 0.05$) in-group II, whereas among MQC-treated groups, no significant change was found. The activity of SOD and catalase in blood serum were found markedly decreased ($p \leq 0.05$) in group II as compared to the untreated control group II. We observed insignificant changes in the activity of SOD and catalase in MQCs exposed groups (Supporting Information 3).

3.12.3. Hematological Profiling. Hematological profiling included red blood cell count (RBCs), total hemoglobin (Hb), white blood cells count (WBCs), mean corpuscular hemoglobin concentration (MCHC), platelet count (PLT), mean corpuscular hemoglobin (MCH), mean corpuscular volume (MCV), and hematocrit value (HCT). No significant change in these parameters of the MQCs treated groups was observed when compared to the negative control group (Supporting Information 3; S5, S6), while the group II treated with MoS_2 QDs had shown altered hematological profile (Supporting Information 3; S5, S6). The said differences in the profile may be due to the interaction of MoS_2 QDs with blood cells leading to the provocation of various immunological cascades such as inflammation, which ultimately altered the hematological parameters.[41]

3.12.4. Oxidative Stress Analysis. To evaluate the toxicity imparted by MQCs and MoS_2 QDs, we evaluated the antioxidative indicators in the vital organs like liver and kidney. The protein content and the enzyme activities results have been summed up in Supporting Information 3; S7, S8. The lipid peroxidation level, measured by the malondialdehyde assay (Supporting Information 3; S8), clearly reveals an insignificant increase in MQCs treated groups compared to the untreated control. However, a significant increase in the lipid peroxidation level was noted in MoS_2 QDs treated positive control group ($p < 0.05$). The superoxide dismutase (SOD) and the catalase activities (CAT) have shown a significant decrease in MoS_2 treated group II ($p < 0.05$), while none of the MQCs treated groups has shown significant decrease in SOD and CAT activities as compared to the control group ($p > 0.05$) (Supporting Information 3; S8).

The results obtained clearly show that even administering the higher dose of MQCs, no significant reduction in the levels of SOD, CAT activities were manifested (Supporting Information 3; S8), while its counterpart, MoS_2 QDs, triggered excessive production of reactive oxygen species (ROS) as evident from the significant decrease in the activities of the said enzymes.[42−44]

Our results are in accordance with other *in vivo* studies using different nanomaterials that possess the ability to elevate the oxidative stress. Similar to the findings pertaining to the use of TiO_2 QDs, our results also confirm the increase in the hepatic injuries and significant alteration in antioxidants level when exposed to the MoS_2 QDs.[40,42] A plethora of literature documents the decrease in SOD activity due to excessive superoxide radical formation and H_2O_2 accumulation.[42,43] Liver is primarily involved in xenobiotic metabolism, which helps detoxification; therefore, it is always on high risk with regard to the reactive oxygen species (free radical) attack, which may lead to lipid peroxidation.[42,45] Numerous other studies also support lipid peroxidation via free radical generation due to nanoparticles induced toxicity.[46] Our results are also in accordance with another earlier report that MoS_2 increased lipid peroxidation in rats. Lipids are the most susceptible macromolecules to oxidative stress, and our results showed that the level of lipid peroxides, measured in terms of MDA, significantly increased due to MoS_2 QDs exposure, which indicated tissue damage.[46] In this study, MQCs were observed to significantly reduce the LPs level by scavenging free radicals and inhibiting the propagating chain reaction of LPs.

MoS_2 QDs administration resulted in an upsurge in the level of free radicals, which in turn engendered cellular damage, and

DOI: 10.1021/acs.chemrestox.9b00135
Chem. Res. Toxicol. 2019, 32, 1599−1618

this observation could be substantiated by the low levels of free radical scavenging enzymes such as catalase and superoxide dismutase that formed the first line of cellular defense against the oxidation injury.[47] On the contrary, MQCs had not depleted the pool of the said enzymes rather proved beneficial in restoring the levels of both enzymes comparable to the control groups, which depicts its nontoxicity. Even the Joint FAO/WHO Expert Committee on Food Additives (JECFA) has assessed the toxicity of curcumin and its intake was declared NOAEL (no observed adverse effect level) up to 250−320 mg/kg body weight per day.[48,49]

In the present study, the *in vitro* toxicity profiling of MQCs has been done in the range of 2−1024 μg/mL and is observed to be nontoxic. MQCs were found highly effective as both antibacterial and antibiofilm agents even at 0.125 μg/mL, while they were found nontoxic at the concentration as high as 1024 μg/mL. Similarly, the animal model experiment revealed their biocompatibility even at concentration 10 mg/kg body weight. However, their counterpart MoS_2 QDs imparted significant toxicity.

3.12.5. Histopathological Investigations of Toxicity. The histopathological sections of liver, kidney, and spleen were observed to access the morphological changes. Figure 16 summarizes the histological status of each organ in respective groups.

The microscopic observations of the liver of the untreated control group (Figure 16A′) reveal the normal structure and compact arrangement of hepatocytes. No obvious hepatic damage was observed in MQCs treated groups III, IV, and V in comparison to the untreated control group I. However, we observed many marked morphological alterations in the liver tissues of the MoS_2 QDs treated group II such as degeneration of hepatocytes, mild necrosis, partial damage of the central vein, hydropic degeneration, and hepatocyte vacuolations (Figure 16B′) as compared to the untreated control group I. Interestingly, the highest treated MQCs group was almost same as that of untreated control (Figure 16C′).

Similarly, the histopathological study of kidney sections showed no remarkable alteration(s) in the highest dosed MQCs treated group VI as compared to the control group I (Figure 16C″). However, the sections of the kidney of MoS_2 QDs treated groups showed mild nephrotoxicity such as swelling of the glomerulus and decreased bowman's space (Figure 16B″). Interestingly, none of the sections of spleen in MoS_2 and MQCs treated groups showed any significant pathological alteration, as compared to the control group (Figure 16A−C).

Liver-specific macrophages are Kupffer cells, which protect liver from hazardous chemicals and materials. However, this leads to the activation of these cells, which induce the generation of reactive oxygen species (ROS).[50] The same pattern of toxicity is perceived in kidneys. A recent report from Zhao et al. suggests that abdominal administration of nanoanatase TiO_2 in mice causes renal toxicity due to excessive generation of ROS, which leads lipid peroxidation and failure of antioxidant defense mechanism.[42]

The results obtained from our study showed that upon oral administration of MoS_2 QDs, we noted obvious signs of hepato and nephro-toxicity such as vacuolation and degeneration of hepatocytes, necrosis, damage to the central vein, hydropic degeneration, and swelling of glomerulus and increase in Bowman's space diameter. Interestingly, no evidence of hepato- and nephrotoxicity was observed after exposure to the hybrid MQCs.

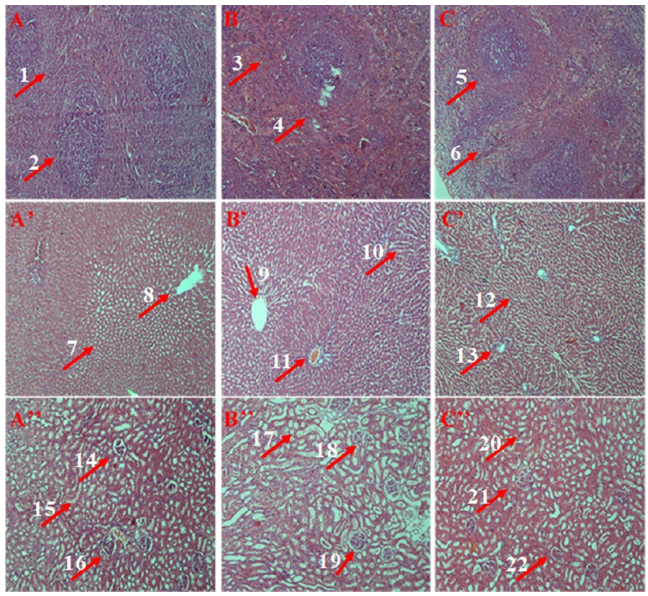

Figure 16. Histopathological evaluation (HE staining, 10×) of various organs (spleen, liver, and kidney) of Charles Foster strain rats treated with MQCs and MoS_2 QDs. A, A′, and A″ are spleen, liver, and kidney of untreated control group I; B, B′, and B″ are spleen, liver, and kidney of MoS_2 QDs treated group II; and C, C′, and C″ are spleen, liver, and kidney of Group VI (highest dosed group). Labels on the images indicate regions of the tissues. (1) White pulp of the group I. (2) Red pulp of the group I. (3) Intact white pulp of group II. (4) Necrotized red pulp of group II. (5) Intact white pulp of the group VI. (6) Intact red pulp of the group VI. (7) Compact and healthy hepatocytes of group I. (8) Undamaged central vein of group I. (9) Dilated central vein of group II. (10) Degenerated, necrotized, vacuolated, and diffused hepatocytes of group II. (11) Damaged central vein. (12) Compact and healthy hepatocytes of group VI. (13) Undamaged central vein of group I. (14, 16) Healthy glomerulus and Bowman's space of group I. (15) Healthy and undistorted loops of group I. (17) Distorted loops of group II. (18, 19) Swollen glomerulus and increased Bowman's space of group II. (20) Healthy and undistorted loops of group VI. (21, 22) Unswollen glomerulus and undilated Bowman's space of group VI.

3.13. Mechanism of MQCs Bactericidal Activities.

Curcumin being a highly hydrophobic moiety and endowed with intrinsic feature to form multiple hydrogen bonds, its strong interactions with lipid bilayers cannot be overruled. Recent report by Leite et al. puts forth the selectivity and protective role of curcumin on eukaryotic system where the cholesterol:phospholipid ratio is more than 40. They reported that the partitioning of curcumin into lipid bilayers had the strongest affinity for phosphatidyl choline (PC) and PC/Chol 80:20, which were reduced significantly by increase of cholesterol to 40%. They further reported the attenuation of curcumin's affinity for partitioning with the increased proportion of phosphatidyl serine (10%) and by the presence of sphingomyelin (20%).[51] These structural features are the hallmarks of eukaryotic cells.

Possibly the bactericidal activities of MQCs could be attributed to the phenolic and the methoxy groups in combination with the β-diketone conjugated diene system having methylene group of the curcumin moiety present. The molecular action of MQCs we observed (fluidity changes and membrane depolarization) could be explained as the resultant of overall neutralization of the positive charges present at the cell surface along with higher order of interaction of curcumin part with hydrophobic domains/amino acids of the cell membrane.

DOI: 10.1021/acs.chemrestox.9b00135
Chem. Res. Toxicol. 2019, 32, 1599−1618

When the negatively charged MQCs interact electrostatically with the membrane, they compete for the positively charged sites (such as phosphatidyl ethanolamine etc. groups) at the outer membrane leaflet of *Klebsiella pneumoniae*. Because the MQCs are bigger than water molecules and carry more negative charges, their binding energy to the membrane is anticipated to be higher than that of water molecules. At physiological temperature, the more and more positive sites on the membrane are exposed (due to the increased thermal movement of phospholipids), and, correspondingly, more and more MQCs are attached. Once they penetrate the membrane, due to their large volume, the MQCs hinder the thermal movement of phospholipids and of the fluorescent probe (DPH); this is reflected in the observed insensitivity of the fluorescence signals. Besides, after *in silico* study, we found strong interaction between curcumin moiety and MlaA and OmpF (outer membrane protein F cursor) trimeric complex system that is needed (Mla system) essentially for asymmetry maintenance of cell membrane via phospholipid extraction. This electrostatic interaction, evoked in many previous investigations of drug treated lipid bilayers, thus seems a good explanation of our observations.

Another more prominent feature of the living cell is the presence of membrane potential. Negative inside, it provides a driving force for the drug to challenge the cell entry. Recent report proves the essentiality of maintained membrane potential in cell survival in case of *Staphylococcus aureus* that was challenged by aminoglycoside. Aminoglycoside lethality was found proportional to the magnitude of the membrane potential.[52]

Earlier fluorescence microscopic investigations showed that cellular uptake of curcumin is higher in tumor cells than in normal cells. The studies also showed that curcumin was maximally distributed in the cell membrane and the nucleus. Second, the glutathione levels in tumor cells tend to be lower than normal cells, thus enhancing the sensitivity of tumor cells to curcumin. Reports suggest that low concentrations of curcumin may protect hepatocytes by reducing lipid peroxidation and cytochrome c release. Conversely, higher concentrations provoke glutathione depletion, caspase-3 activation, and hepatocytotoxicity.[53]

Our results show that the presence of MQCs induces a greater susceptibility of the cell membrane to disorganization in terms of acyl shifting (the shielding of the superficial membrane positive and zwitterion charges) and dynamics (in liquid crystalline phase), which facilitate their self-intrusion across the thickness that eventually lead to the ooze out of the cytosolic contents. This would be the most important biomedical consequence of the drug induced membrane organization changes we report in this paper.

4. CONCLUSIONS

In recent years, considerable efforts have been put toward development/synthesis of new safer and efficient antimicrobial agents. In the current study, we demonstrated a facile and eco-friendly synthesis for the development of MQCs, a novel theranostic hybrid, as a new potential therapeutic agent for the treatment of hypervirulent *Klebsiella pneumoniae* infections. The synthesized sample was characterized structurally and spectroscopically using TEM, AFM, Raman spectroscopy, and XPS. Average particle sizes of the MQCs were found to be ∼13 nm, and they exhibited excellent photophysical properties with emission QY ≈ 2.71%. Moreover, there was an excellent chemosensitizing effect of MQCs as evident by its greater bactericidal efficiency. Additionally, we explored and reported its mode of action using fluorescent probes for studying membrane dynamics, permeabilization, and its depolarization. This approach simplifies and expands the arsenal of preparation methods for such drugs and their target exploration. We further demonstrated that MQCs might potentially be used as targeted nanotheranostic agent that simultaneously affects the bacterial survival and the biofilm biogenesis. Furthermore, we also demonstrated the biocompatibility of MQCs both *in vitro* and *in vivo*. Distribution and organ-specific accumulation of MQCs were also investigated after oral administration into rats to ensure its biocompatibility. In all, the current study demonstrates the synthesis and application of MoS_2 fabricated curcumin quantum dots. Taken together, these MQCs represent a new generation of therapeutic agents, providing potential antibacterial and antibiofilm activities against drug-resistant and high slime producing organisms without imparting cytotoxicity to the eukaryotic systems. The combination of these two components in a single molecule maximized the preclinical antibacterial and antibiofilm outcomes of these nanostructures. Apart from their potential promise as bioimaging aid and as a theranostic candidate, substantial improvements in exploring standardized downstream processing techniques with high efficiency and robust yield, scalable production, storage, and understanding *in vivo* trafficking of MQCs in humans are the issues necessary to be dealt with before their clinical translation as a drug.

■ ASSOCIATED CONTENT

Supporting Information

The Supporting Information is available free of charge on the ACS Publications website at DOI: 10.1021/acs.chemrestox.9b00135.

Details of synthesis and characterizations of MoS_2 QDs, TRPL fitted data of MQCs, quantum yield calculation, FTIR-ATR data of MQCs and detailed *in vivo* evaluation of cytotoxicity imparted by MQCs (PDF)

■ AUTHOR INFORMATION

Corresponding Author

*E-mail: pradyotbhu@gmail.com.

ORCID

Himanshu Mishra: 0000-0002-5804-6840
Anchal Srivastava: 0000-0002-6573-5345
Pradyot Prakash: 0000-0003-3622-4295

Author Contributions

●A.K.S., H.M., Z.F., and S.Y. contributed equally to this work. A.K.S. and P.P. conceived, designed, and analyzed results of the study. A.K.S., S.Y., and A.K.P. designed, performed the cultivation experiments and performed susceptibility experiments, bacterial growth rate analysis, along with biofilm degradation assay. A.K.S., H.M., Z.F., P.A., K.V., and A.S. performed experiments on synthesis, physical characterizations, and analyzed data. A.K.S., N.N., and B.S.C. performed confocal microcopy experiments and analyzed the data. A.K.S., S.Y., and K.N. performed *in vitro* toxicity assay, while Z.F. and P.A. performed animal experiments. A.K.S. and A.G.K. did histopathological evaluations, while A.K.S., S.Y., and K.S. performed and analyzed results with flow cytometry. P.B.

DOI: 10.1021/acs.chemrestox.9b00135
Chem. Res. Toxicol. 2019, 32, 1599−1618

performed and analyzed *in silico* studies along with A.K.S. A.K.S. wrote the manuscript, which was consented by all the coauthors.

Funding

We sincerely acknowledge the financial support from University Grants Commission, New Delhi for the contingency grant offered to A.K.S. as SRF [2061430918 vide 22/06/2014(i) EU-V], S.Y. as JRF [1121630870 vide 18/12/2016(ii)EU-V], and H.M. as SRF [Letter No. 09/013/(0752)/2018-EMR-I] CSIR, New Delhi. Besides, we sincerely acknowledge the DST-PURSE grant sanctioned to Department of Microbiology, IMS, BHU.

Notes

The authors declare no competing financial interest.

■ ACKNOWLEDGMENTS

We acknowledge Dr. Vinod Kumar Tiwari, Assoc. Prof., Dept. of Chemistry, Institute of Science for facilitation and valuable discussions on *in silico* studies. Besides, we are thankful to the priceless efforts in histological study facilitation made by the technical staff members Dinesh Kumar, Kanhaiya Lal, and Bhagyalakshmi of Department of Pathology, Institute of Medical Sciences, Banaras Hindu University, Varanasi.

■ REFERENCES

(1) Shon, A. S., Bajwa, R. P. S., and Russo, T. A. (2013) Hypervirulent (Hypermucoviscous) Klebsiella Pneumoniae: A New and Dangerous Breed. *Virulence 4* (2), 107−118.

(2) Harada, S., and Doi, Y. (2018) Hypervirulent Klebsiella Pneumoniae: A Call for Consensus Definition and International Collaboration. *J. Clin. Microbiol. 56* (9), e00959−18.

(3) Davies, B. W., and Fante, R. G. (2016) Concurrent Endophthalmitis and Orbital Cellulitis from Metastatic Klebsiella Pneumonia Liver Abscess. *Ophthal. Plast. Reconstr. Surg. 32* (5), e118−e119.

(4) Pomakova, D. K., Hsiao, C. B., Beanan, J. M., Olson, R., MacDonald, U., Keynan, Y., and Russo, T. A. (2012) Clinical and Phenotypic Differences between Classic and Hypervirulent Klebsiella Pneumonia: An Emerging and under-Recognized Pathogenic Variant. *Eur. J. Clin. Microbiol. Infect. Dis. 31* (6), 981−989.

(5) Indira Priyadarsini, K. (2013) Chemical and Structural Features Influencing the Biological Activity of Curcumin. *Curr. Pharm. Des. 19* (11), 2093−2100.

(6) Singh, A. K., Prakash, P., Singh, R., Nandy, N., Firdaus, Z., Bansal, M., Singh, R. K., Srivastava, A., Roy, J. K., Mishra, B., et al. (2017) Curcumin Quantum Dots Mediated Degradation of Bacterial Biofilms. *Front. Microbiol. 8*, 1517.

(7) Singh, A. K., Yadav, S., Sharma, K., Firdaus, Z., Aditi, P., Neogi, K., Bansal, M., Gupta, M. K., Shanker, A., Singh, R. K., et al. (2018) Quantum Curcumin Mediated Inhibition of Gingipains and Mixed-Biofilm of Porphyromonas Gingivalis Causing Chronic Periodontitis. *RSC Adv. 8* (70), 40426−40445.

(8) Yang, J., Luo, M., Tan, Z., Dai, M., Xie, M., Lin, J., Hua, H., Ma, Q., Zhao, J., and Liu, A. (2017) Oral Administration of Nano-Titanium Dioxide Particle Disrupts Hepatic Metabolic Functions in a Mouse Model. *Environ. Toxicol. Pharmacol. 49*, 112−118.

(9) Lin, H., Wang, C., Wu, J., Xu, Z., Huang, Y., and Zhang, C. (2015) Colloidal Synthesis of MoS 2 Quantum Dots: Size-Dependent Tunable Photoluminescence and Bioimaging. *New J. Chem. 39* (11), 8492−8497.

(10) Dong, H., Tang, S., Hao, Y., Yu, H., Dai, W., Zhao, G., Cao, Y., Lu, H., Zhang, X., and Ju, H. (2016) Fluorescent MoS_2 Quantum Dots: Ultrasonic Preparation, up-Conversion and down-Conversion Bioimaging, and Photodynamic Therapy. *ACS Appl. Mater. Interfaces 8* (5), 3107−3114.

(11) Mishra, H., Singh, S. K., Singh, V. K., Singh, J., Srikrishna, S., and Srivastava, A. (2018) Highly Stable and Bio-Compatible Luminescent Molybdenum Disulfide Quantum Dots for Imaging of Alimentary Canal in Drosophila. *J. Lumin. 202*, 111−117.

(12) Yin, W., Yu, J., Lv, F., Yan, L., Zheng, L. R., Gu, Z., and Zhao, Y. (2016) Functionalized Nano-MoS_2 with Peroxidase Catalytic and near-Infrared Photothermal Activities for Safe and Synergetic Wound Antibacterial Applications. *ACS Nano 10* (12), 11000−11011.

(13) Awasthi, G. P., Adhikari, S. P., Ko, S., Kim, H. J., Park, C. H., and Kim, C. S. (2016) Facile Synthesis of ZnO Flowers Modified Graphene like MoS_2 Sheets for Enhanced Visible-Light-Driven Photocatalytic Activity and Antibacterial Properties. *J. Alloys Compd. 682*, 208−215.

(14) Martinez, E., Engel, E., Planell, J. A., and Samitier, J. (2009) Effects of Artificial Micro-and Nano-Structured Surfaces on Cell Behaviour. *Ann. Anat. 191* (1), 126−135.

(15) Jiang, W., Kim, B. Y. S., Rutka, J. T., and Chan, W. C. W. (2008) Nanoparticle-Mediated Cellular Response Is Size-Dependent. *Nat. Nanotechnol. 3* (3), 145.

(16) Nel, A. E., Mädler, L., Velegol, D., Xia, T., Hoek, E. M. V, Somasundaran, P., Klaessig, F., Castranova, V., and Thompson, M. (2009) Understanding Biophysicochemical Interactions at the Nano−bio Interface. *Nat. Mater. 8* (7), 543.

(17) Linton, R. H., Carter, W. H., Pierson, M. D., and Hackney, C. R. (1995) Use of a Modified Gompertz Equation to Model Nonlinear Survival Curves for Listeria Monocytogenes Scott A. *J. Food Prot. 58* (9), 946−954.

(18) Wilson, D. L. (1994) The Analysis of Survival (Mortality) Data: Fitting Gompertz, Weibull, and Logistic Functions. *Mech. Ageing Dev. 74* (1−2), 15−33.

(19) Singh, A. K., Prakash, P., Achra, A., Singh, G. P., Das, A., and Singh, R. K. (2017) Standardization and Classification of In Vitro Biofilm Formation by Clinical Isolates of Staphylococcus Aureus. *J. Glob. Infect. Dis. 9* (3), 93.

(20) Singh, A. K., Yadav, S., Chauhan, B. S., Nandy, N., Singh, R., Neogi, K., Roy, J. K., Srikrishna, S., Singh, R. K., and Prakash, P. (2019) Classification of Clinical Isolates of Klebsiella Pneumoniae Based on Their in Vitro Biofilm Forming Capabilities and Elucidation of the Biofilm Matrix Chemistry with Special Reference to the Protein Content. *Front. Microbiol. 10*, 669.

(21) Yun, J., Lee, H., Ko, H. J., Woo, E.-R., and Lee, D. G. (2015) Fungicidal Effect of Isoquercitrin via Inducing Membrane Disturbance. *Biochim. Biophys. Acta, Biomembr. 1848* (2), 695−701.

(22) Kim, W., Conery, A. L., Rajamuthiah, R., Fuchs, B. B., Ausubel, F. M., and Mylonakis, E. (2015) Identification of an Antimicrobial Agent Effective against Methicillin-Resistant Staphylococcus Aureus Persisters Using a Fluorescence-Based Screening Strategy. *PLoS One 10* (6), e0127640.

(23) Grace, J. L., Huang, J. X., Cheah, S.-E., Truong, N. P., Cooper, M. A., Li, J., Davis, T. P., Quinn, J. F., Velkov, T., and Whittaker, M. R. (2016) Antibacterial Low Molecular Weight Cationic Polymers: Dissecting the Contribution of Hydrophobicity, Chain Length and Charge to Activity. *RSC Adv. 6* (19), 15469−15477.

(24) Moreland, J. L., Gramada, A., Buzko, O. V., Zhang, Q., and Bourne, P. E. (2005) The Molecular Biology Toolkit (MBT): A Modular Platform for Developing Molecular Visualization Applications. *BMC Bioinf. 6* (1), 21.

(25) Morris, G. M., Goodsell, D. S., Halliday, R. S., Huey, R., Hart, W. E., Belew, R. K., and Olson, A. J. (1998) Automated Docking Using a Lamarckian Genetic Algorithm and an Empirical Binding Free Energy Function. *J. Comput. Chem. 19* (14), 1639−1662.

(26) Vichai, V., and Kirtikara, K. (2006) Sulforhodamine B Colorimetric Assay for Cytotoxicity Screening. *Nat. Protoc. 1* (3), 1112.

(27) Freyer, D., and Harms, C. (2017) Kinetic Lactate Dehydrogenase Assay for Detection of Cell Damage in Primary Neuronal Cell Cultures. *J. Neurosci.*, DOI: 10.21769/BioProtoc.2308.

(28) Ingolfsson, H. I., Koeppe, R. E., and Andersen, O. S. (2007) Curcumin Is a Modulator of Bilayer Material Properties. *Biochemistry 46* (36), 10384−10391.

(29) Alsop, R. J., Dhaliwal, A., and Rheinstädter, M. C. (2017) Curcumin Protects Membranes through a Carpet or Insertion Model Depending on Hydration. *Langmuir 33* (34), 8516−8524.

DOI: 10.1021/acs.chemrestox.9b00135
Chem. Res. Toxicol. 2019, 32, 1599−1618

(30) Lyu, Y., Xiang, N., Mondal, J., Zhu, X., and Narsimhan, G. (2018) Characterization of Interactions between Curcumin and Different Types of Lipid Bilayers by Molecular Dynamics Simulation. *J. Phys. Chem. B 122* (8), 2341−2354.
(31) Snijder, H. J., Ubarretxena-Belandia, I., Blaauw, M., Kalk, K. H., Verheij, H. M., Egmond, M. R., Dekker, N., and Dijkstra, B. W. (1999) Structural Evidence for Dimerization-Regulated Activation of an Integral Membrane Phospholipase. *Nature 401* (6754), 717.
(32) Bishop, R. E., Gibbons, H. S., Guina, T., Trent, M. S., Miller, S. I., and Raetz, C. R. H. (2000) Transfer of Palmitate from Phospholipids to Lipid A in Outer Membranes of Gram-negative Bacteria. *EMBO J. 19* (19), 5071−5080.
(33) Malinverni, J. C., and Silhavy, T. J. (2009) An ABC Transport System That Maintains Lipid Asymmetry in the Gram-Negative Outer Membrane. *Proc. Natl. Acad. Sci. U. S. A. 106* (19), 8009−8014.
(34) Chong, Z., Woo, W., and Chng, S. (2015) Osmoporin OmpC Forms a Complex with MlaA to Maintain Outer Membrane Lipid Asymmetry in E Scherichia Coli. *Mol. Microbiol. 98* (6), 1133−1146.
(35) Thong, S., Ercan, B., Torta, F., Fong, Z. Y., Wong, H. Y. A., Wenk, M. R., and Chng, S.-S. (2016) Defining Key Roles for Auxiliary Proteins in an ABC Transporter That Maintains Bacterial Outer Membrane Lipid Asymmetry. *eLife 5*, e19042.
(36) Zhao, L., Gao, X., Liu, C., Lv, X., Jiang, N., and Zheng, S. (2017) Deletion of the VacJ Gene Affects the Biology and Virulence in Haemophilus Parasuis Serovar 5. *Gene 603*, 42−53.
(37) Suzuki, T., Murai, T., Fukuda, I., Tobe, T., Yoshikawa, M., and Sasakawa, C. (1994) Identification and Characterization of a Chromosomal Virulence Gene, VacJ, Required for Intercellular Spreading of Shigella Flexneri. *Mol. Microbiol. 11* (1), 31−41.
(38) Shen, L., Gao, X., Wei, J., Chen, L., Zhao, X., Li, B., and Duan, K. (2012) PA2800 Plays an Important Role in Both Antibiotic Susceptibility and Virulence in Pseudomonas Aeruginosa. *Curr. Microbiol. 65* (5), 601−609.
(39) Abellón-Ruiz, J., Kaptan, S. S., Baslé, A., Claudi, B., Bumann, D., Kleinekathöfer, U., and van den Berg, B. (2017) Structural Basis for Maintenance of Bacterial Outer Membrane Lipid Asymmetry. *Nat. Microbiol. 2* (12), 1616.
(40) Li, S.-Q., Zhu, R.-R., Zhu, H., Xue, M., Sun, X.-Y., Yao, S.-D., and Wang, S.-L. (2008) Nanotoxicity of TiO2 Nanoparticles to Erythrocyte in Vitro. *Food Chem. Toxicol. 46* (12), 3626−3631.
(41) Shin, S.-H., Ye, M.-K., Kim, H.-S., and Kang, H.-S. (2007) The Effects of Nano-Silver on the Proliferation and Cytokine Expression by Peripheral Blood Mononuclear Cells. *Int. Immunopharmacol. 7* (13), 1813−1818.
(42) Liu, H., Ma, L., Liu, J., Zhao, J., Yan, J., and Hong, F. (2010) Toxicity of Nano-Anatase TiO2 to Mice: Liver Injury, Oxidative Stress. *Toxicol. Environ. Chem. 92* (1), 175−186.
(43) Kim, S., Choi, J. E., Choi, J., Chung, K.-H., Park, K., Yi, J., and Ryu, D.-Y. (2009) Oxidative Stress-Dependent Toxicity of Silver Nanoparticles in Human Hepatoma Cells. *Toxicol. In Vitro 23* (6), 1076−1084.
(44) Nel, A., Xia, T., Mädler, L., and Li, N. (2006) Toxic Potential of Materials at the Nanolevel. *Science (Washington, DC, U. S.) 311* (5761), 622−627.
(45) Patlolla, A., McGinnis, B., and Tchounwou, P. (2011) Biochemical and Histopathological Evaluation of Functionalized Single-walled Carbon Nanotubes in Swiss−Webster Mice. *J. Appl. Toxicol. 31* (1), 75−83.
(46) Erdem, A., Metzler, D., Cha, D. K., and Huang, C. P. (2015) The Short-Term Toxic Effects of TiO 2 Nanoparticles toward Bacteria through Viability, Cellular Respiration, and Lipid Peroxidation. *Environ. Sci. Pollut. Res. 22* (22), 17917−17924.
(47) Halliwell, B., and Gutteridge, J. M. C. (2015) *Free Radicals in Biology and Medicine*, Oxford University Press.
(48) Kocaadam, B., and Şanlier, N. (2017) Curcumin, an Active Component of Turmeric (Curcuma Longa), and Its Effects on Health. *Crit. Rev. Food Sci. Nutr. 57* (13), 2889−2895.
(49) Authority, E. F. S. (2014) Refined Exposure Assessment for Curcumin (E 100). *EFSA J. 12* (10), 3876.
(50) Roberts, R. A., Ganey, P. E., Ju, C., Kamendulis, L. M., Rusyn, I., and Klaunig, J. E. (2006) Role of the Kupffer Cell in Mediating Hepatic Toxicity and Carcinogenesis. *Toxicol. Sci. 96* (1), 2−15.
(51) Leite, N. B., Martins, D. B., Fazani, V. E., Vieira, M. R., and dos Santos Cabrera, M. P. (2018) Cholesterol Modulates Curcumin Partitioning and Membrane Effects. *Biochim. Biophys. Acta, Biomembr. 1860* (11), 2320−2328.
(52) Hurdle, J. G., O'Neill, A. J., Chopra, I., and Lee, R. E. (2011) Targeting Bacterial Membrane Function: An Underexploited Mechanism for Treating Persistent Infections. *Nat. Rev. Microbiol. 9* (1), 62−75.
(53) Ghoneim, A. I. (2009) Effects of Curcumin on Ethanol-Induced Hepatocyte Necrosis and Apoptosis: Implication of Lipid Peroxidation and Cytochrome C. *Naunyn-Schmiedeberg's Arch. Pharmacol. 379* (1), 47.

DOI: 10.1021/acs.chemrestox.9b00135
Chem. Res. Toxicol. 2019, 32, 1599−1618